A Novel Algorithm for Detecting Lake-Breeze Fronts at Lake Victoria Using Station Observations

MUSA SSEMUJJU,[a,b] MARLON MARANAN,[a] ANDREAS H. FINK,[a] AND SIMON AGEET[a]

[a] *Institute of Meteorology and Climate Research Troposphere Research (IMKTRO), Karlsruhe Institute of Technology, Karlsruhe, Germany*

[b] *Uganda Department of Meteorological Services, Kampala, Uganda*

(Manuscript received 31 December 2025, in final form 22 April 2026, accepted 8 May 2026)

ABSTRACT: Lake Victoria (LV), the world's largest tropical lake, significantly influences East Africa's regional climate through diurnally varying lake–land-breeze circulations. In particular, lake-breeze fronts (LBFs) often trigger cloudiness, deep moist convection, and heavy precipitation, leading to weather-related hazards. To systematically study LBFs over LV, we developed an observation-based lake-breeze detection algorithm (OLBDA), which objectively identifies LBF passages using 15-min data from 45 automatic weather stations across Uganda's extended coastal region over 6 years (2017–22). Focusing on daytime (0900–1900 LT) during dry months (December–February and June–August), the algorithm applies thresholds based on the lowest (highest) 30% of temperature drops (dewpoint and wind speed increases), enabling detection of subtle meteorological changes associated with LBF passage. Validation against visible satellite imagery shows strong performance with high accuracy (ACC = 0.76), detection rate [probability of detection (POD) > 0.7], and low false alarms [probability of false alarm (POFA) = 0.2]. Application of the OLBDA revealed that LBFs predominantly occur from early afternoon to evening, peaking at 1300 LT near the coast and shifting inland with distance. LBFs were observed on 48% of days, with December–February and January having the highest seasonal and monthly frequencies, respectively. LBF propagation speed varied in relation to the background wind in different hinterland sectors of LV, with the fastest movement westward at 8 m s^{-1} and the slowest northward at 5.8 m s^{-1}. LBFs penetrate up to ~130 km inland. The OLBDA offers a robust framework for analyzing LBFs, providing valuable insights for disaster preparedness and climate mitigation in the Lake Victoria basin.

KEYWORDS: Inland seas/lakes; Sea breezes; Algorithms; Automatic weather stations

1. Introduction

A large and growing proportion of the global population lives within 150 km of the ocean and lake coastlines, where many megacities are located (Small and Cohen 2004; Cosby et al. 2024). These regions are particularly susceptible to land–sea and land–lake-breeze (LSB/LLB) circulations, which greatly impact cloud development (van der Linden et al. 2015; Viner et al. 2021; Wermter et al. 2022), deep convective initiation, and related (extreme) rainfall events (Mapes et al. 2003a,b; Warner et al. 2003; Miller et al. 2003; Birch et al. 2015; Fu et al. 2022). The LSBs and LLBs also impact air quality through pollutant transport and dispersion (Zhang et al. 2007; Loughner et al. 2011, 2014; Stauffer et al. 2015; Deroubaix et al. 2019) and shaping local climate patterns (e.g., Dai et al. 1999). Despite their importance, LSBs and LLBs and their associated impacts remain poorly understood and inadequately represented in most global climate models (Hannak et al. 2017), partly due to the coarse resolution and insufficient and/or inadequate observational data for assimilation. These model deficiencies contribute to substantial uncertainties in projections of future coastal climate and rainfall patterns. This "global" problem is also relevant to Lake Victoria (LV), the second largest lake on Earth and the largest in the tropics. The region surrounding LV is already experiencing devastating extreme rainfall and urban flooding events (Wainwright et al. 2021; Pietroiusti et al. 2024), exacerbated by rapid population growth and escalating pollution levels, which contribute to clogged drainage systems and degradation of natural water management systems. Climate change is expected to aggravate these impacts through even more extreme rainfall events (IPCC 2023; WMO 2025).

LSB and LLB circulations are thermally driven mesoscale (local) systems formed due to pressure gradients between the air over a warmer land surface and the cooler adjacent water body during the day and vice versa at night. These circulations are favored in weak synoptic flow (Miller et al. 2003; Wentworth et al. 2015) and can be triggered by a temperature gradient as low as 1°C (Watts 1955). Larger temperature gradients, often common in dry months, induce stronger sea- or lake-breeze fronts (SBFs/LBFs), the leading edge of the sea/lake breeze, with greater propagation velocity and deeper inland penetration. For instance, sea breezes have been observed to penetrate over 200 km inland in Australia (Simpson 1994; Barry and Chorley 2010) and over 100 km in Brazil, India, and the southeastern United States (Planchon et al. 2006; Muppa et al. 2012; Noble et al. 2024). Over West Africa, Guedje et al. (2019) reported

Denotes content that is immediately available upon publication as open access.

Supplemental information related to this paper is available at the Journals Online website: https://doi.org/10.1175/JAMC-D-25-0253.s1.

Corresponding author: Musa Ssemujju, musa.ssemujju@kit.edu

DOI: 10.1175/JAMC-D-25-0253.1

SBFs reaching 185 km inland, driven by strong temperature and pressure gradients. Importantly, several of these studies have shown strong connections of the LSBs/LLBs to convection initiation.

Over LV, many studies have investigated the climatic drivers of precipitation extremes and severe thunderstorms in the LV basin (LVB; Chamberlain et al. 2014; Thiery et al. 2016; Woodhams et al. 2019; Finney et al. 2020). A key factor identified is the land–lake temperature contrast, which drives region-specific mesoscale circulations and initiates thunderstorms (Flohn and Fraedrich 1966; Anyah et al. 2006; Thiery et al. 2015; Van de Walle et al. 2020). These circulations are governed by diurnal heating, where daytime solar radiation warms the land faster than the lake, generating pressure gradients that initiate afternoon lake breezes and overlake subsidence (Virts and Goodman 2020). The breezes are often enhanced by upslope winds from the Kenyan highlands, particularly along the eastern shore where they interact with prevailing easterlies to strengthen low-level convergence (Thiery et al. 2015; Woodhams et al. 2019). This mesoscale convergence contributes to afternoon deep convection maxima over land, with lightning peaking around 1300–1600 LT and precipitation falling shortly after at around 1500–1800 LT (Virts and Goodman 2020). Collectively, these studies highlight the dominant role of LLB circulation in controlling storm initiation, location, timing, intensity, and propagation, especially during the dry seasons of December–February (DJF) and June–August (JJA). These months are ideal for studying LLBs due to low cloudiness, weak synoptic winds (Ngoma et al. 2021), and stable lake surface temperatures (~25°C) throughout the day (Lumb 1970). The plethora of studies on LLB corroborate that even though the temperature gradient between the lake and the surrounding land is relatively small, it is still sufficient to drive daytime LLBs during the relatively cloud-free dry seasons.

Globally, various methods have been employed to detect SBFs/LBFs, with many studies relying on time series from at least two meteorological stations (e.g., Papanastasiou and Melas 2009; Laird et al. 2001; Azorin-Molina et al. 2011; Stauffer and Thompson 2015; Hughes and Veron 2018; Guedje et al. 2019; Mazzuca et al. 2019; Viner et al. 2021). Typically, data from coastal and inland stations are used to track the inland progression of the breeze front. Visible satellite imagery has also been used (e.g., Schrage and Fink 2012; van der Linden et al. 2015), though its effectiveness is limited under clear-sky conditions. Over LV, studies have examined cloud and precipitation patterns to infer LLB impacts on local weather (Datta 1981; Chamberlain et al. 2014), but persistent convection around the lake complicates clear attribution. Numerical models have also been applied (Anyah et al. 2006; Song et al. 2004), though convection parameterization introduces uncertainty and limits realism in precipitation patterns. More recent work using convection-permitting models (Woodhams et al. 2019, 2022; Finney et al. 2020) has provided detailed insights but remains limited to case studies. Radar observations (Waniha et al. 2019; Wilson and Roberts 2022) revealed interactions between gust fronts and LLBs, yet operational constraints hinder consistent data collection. To this end, the primary bottleneck in developing a ground-based LBF detection algorithm in the region has always been the lack of a dense and reliable in situ network, yet many stations are needed to prove spatial coherency.

Efforts to automate detections worldwide have led to the development of various algorithms that can identify SBFs/LBFs using either station data or satellite images. Most of these algorithms have been developed in extratropical regions (e.g., Berri and Dezzutti 2020; Viner et al. 2021; Stauffer and Thompson 2015; Hughes and Veron 2018; Wentworth et al. 2015; El-Geziry et al. 2021; McCabe and Freedman 2023), with fewer studies in tropical regions (e.g., Guedje et al. 2019; Ferdiansyah et al. 2020; Abatan et al. 2014; Planchon et al. 2006). Wind direction reversal has been commonly used as the primary criterion for identifying sea-/lake-breeze days, though not all SBF/LBF passages exhibit this feature (Guedje et al. 2019). Some are better identified through increases in wind speed, temperature drops, and humidity rises, often using fixed thresholds (e.g., Stauffer et al. 2015; Mazzuca et al. 2019; Sikora et al. 2010; Hughes and Veron 2018; Noble et al. 2024). A key challenge remains in ensuring that the observed changes in the meteorological variables are solely caused by the SBF/LBF passages (Ryznar and Touma 1981). Nonetheless, the algorithms have proven effective, largely due to their objective criteria, reliance on standard meteorological observations, and ease of application to long-term datasets.

With respect to LV, despite the enormous role of LLBs over the LVB and the obvious usefulness of detection algorithms, to the best of our knowledge, no algorithm currently exists for detecting and tracking LBFs using observational data from a dense station network. This gap is largely due to the scarcity of publicly available data around LV, making it hard to develop an automated algorithm in the first place. To address this, the present study develops and evaluates an automated observation-based lake-breeze detection algorithm (OLBDA) using data from an unprecedented dense network of stations, primarily concentrated along the northern shore in Uganda. The specific objectives of this study are to (i) develop an algorithm solely based on ground station observations to detect LBFs and evaluate its ability to accurately identify LBF passages across the study domain, (ii) use the algorithm to analyze the spatiotemporal characteristics of LBFs, and (iii) develop a baseline climatology of LBFs in the region based on algorithm-detected events. This work contributes to the limited body of research on LLB systems over LV and advances understanding of their spatiotemporal characteristics.

The rest of the paper is structured as follows: Section 2 describes the study area and the data used. Section 3 presents the methods used, including the development of the observation-based lake-breeze detection algorithm. Results are presented in section 4, starting with an analysis of the algorithm's performance and then its application to derive the various LBF characteristics and climatology. Finally, section 5 provides a summary and conclusions.

2. Study area and data

a. Description of the study area

The study focuses on the areas surrounding the northern shores of LV including the Kampala metropolitan area in

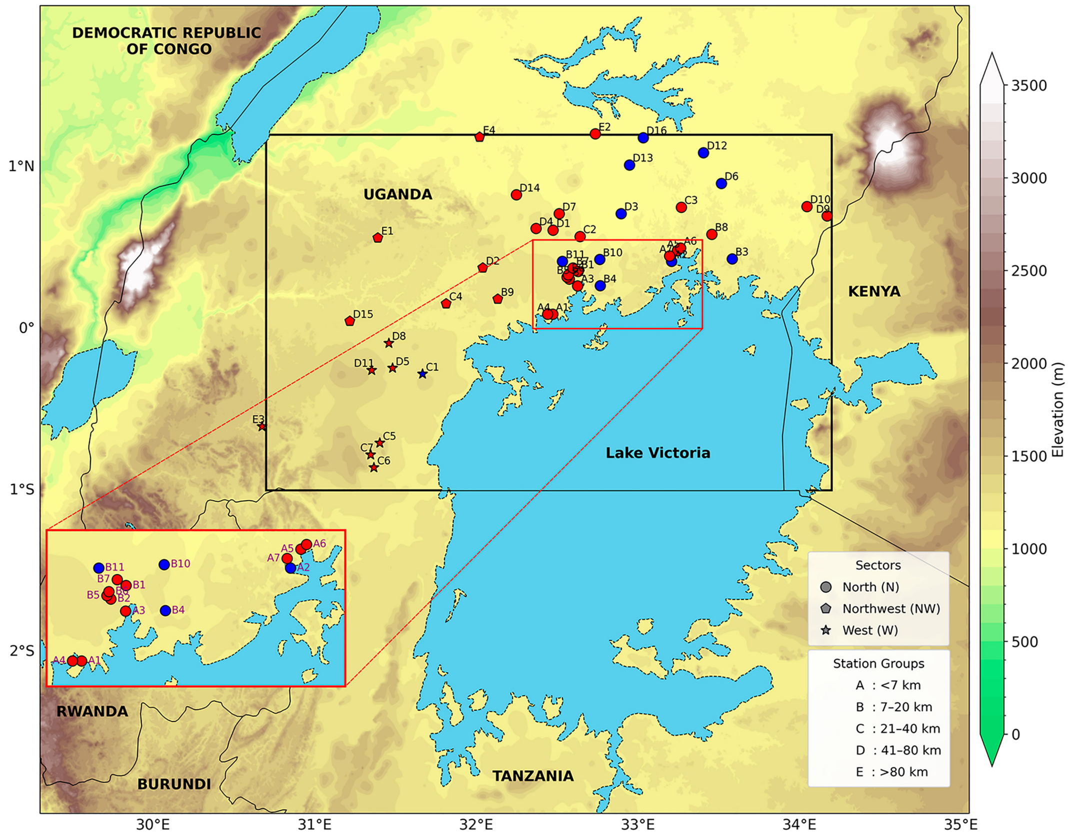

FIG. 1. Map showing the location of LV and the surrounding topography. The study area is shown by the black box together with the distribution of the AWSs: TAHMO (red) and UDMS (blue). Stations are classified according to (a) their relative distances from the coastline (letters A–E) and coastal sector location (markers) (see Table S1 for further information). The color shading shows the elevation from the Global Land One-km Base Elevation Project (GLOBE; Hastings et al. 1999). The inset highlights the location of stations around Kampala and Jinja within the study area (red box).

Uganda (Fig. 1). LV, located in East Africa, is the largest tropical freshwater body in the world, with a surface area of 69 000 km^2 (Semazzi 2011). Straddling the equator, the lake is shared by three East African countries (Uganda, Kenya, and Tanzania) and supports the livelihood of over 30 million people in eastern Africa (Semazzi 2011). The study area is characterized by two distinct rainfall seasons: March–May (MAM), commonly termed the "long rains" with its peak in April, and September–November (SON), commonly known as the "short rains" with its peak in October (Nicholson 2017; Diem et al. 2019). However, the region receives significant rainfall amounts even during the dry months of JJA and DJF. These rains are the result of the local effect of LV, particularly, the LLB circulation system which results in nocturnal and afternoon rainfall regimes in the western and eastern sides of the lake, respectively (Nicholson 2017). In addition, the prevailing surface winds are mostly easterlies, with some seasonal variability due to the movement of the intertropical convergence zone (ITCZ) (Flohn and Fraedrich 1966; Nicholson 1996). Topographically, the area is relatively flat which favors inland penetration of the lake breezes (LBs).

b. *Observational data*

1) IN SITU STATION DATA

High-quality ground-based observations are often essential in any scientific research due to their accuracy and reliability. In this study, in situ data from 45 automatic weather stations (AWSs) located along the northern shores of LV in Uganda within a radius of 100 km from the lake shores are utilized (Fig. 1). Of these, 34 stations are operated by the Trans-African Hydro-Meteorological Observatory (TAHMO; https://tahmo.org; van de Giesen et al. 2014), while the remaining 11 are managed by the Uganda Department of Meteorological Services (UDMS).

The AWSs record several meteorological parameters, including precipitation, air temperature, solar radiation, relative humidity, atmospheric pressure, and wind speed and direction at 15-min intervals. TAHMO data, which have been widely used in previous studies across Africa (e.g., Macharia et al. 2022; Hoeller et al. 2024), were downloaded from the TAHMO data portal (https://portal.tahmo.org/login), while UDMS station data were obtained from UDMS. It is important to note that

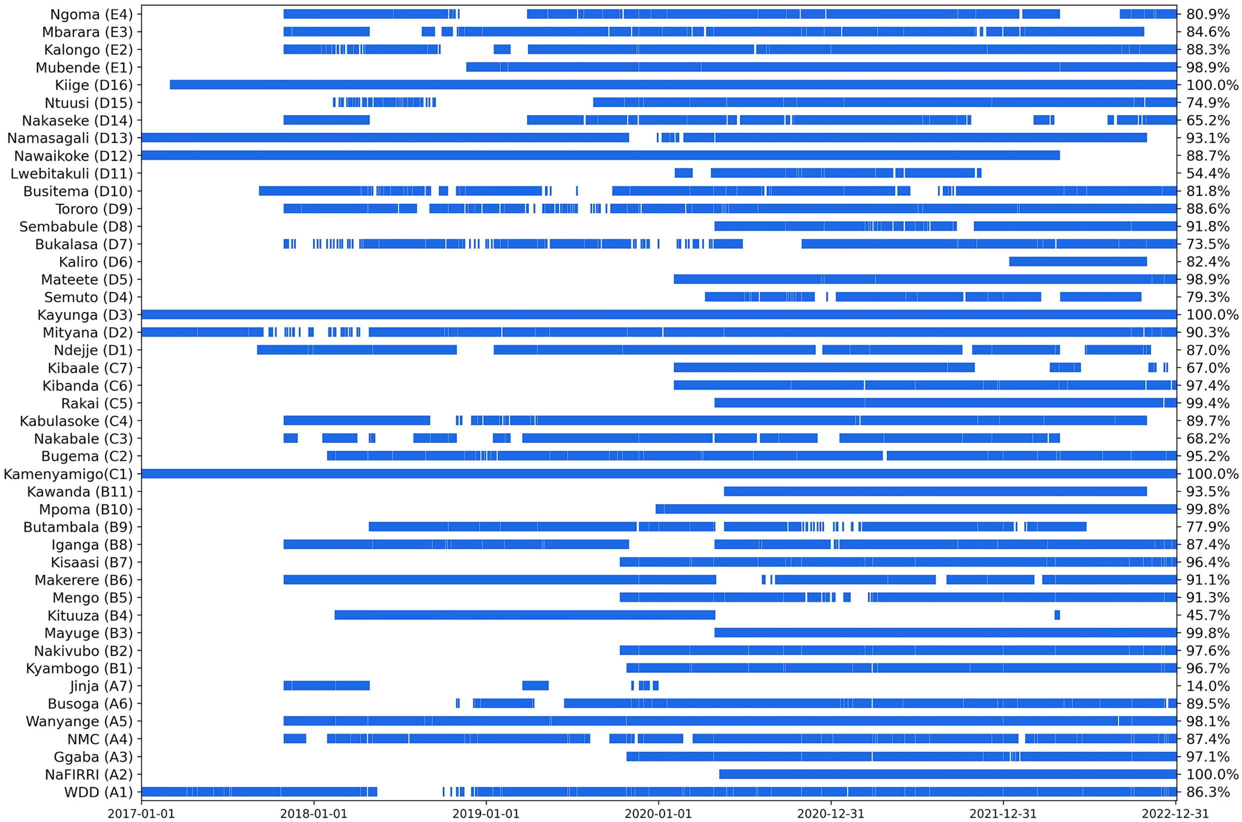

FIG. 2. Temporal availability of the 45 AWS data used in the study for the period 2017–22. The number string in brackets after the station name indicates the station's distance in kilometers from the coast (see Fig. 1). The blue-strip shading shows >80% subdaily data availability based on the 41 time steps from 0900 to 1900 LT (15-min intervals) expressed as percentages (numbers on the right) for each station during the dry seasons of DJF and JJA in the period 2017–22.

both TAHMO and UDMS data used in this study are recorded at a 2-m height above ground level.

Given that some of the UDMS AWS datasets had not previously been used in scientific research, a comprehensive quality control process was undertaken prior to analysis. This included checks for time stamp consistency, range and step tests to flag values outside known climatological bounds, and internal consistency checks for parameters such as wind and temperature. TAHMO applies quality control processes that include cross calibration between sensors, comparisons between nearby stations, and qualitative intercomparisons with satellite observations (van de Giesen et al. 2014; Macharia et al. 2022).

Considering the tropical climate of the study area, which is characterized by alternating wet and dry seasons, LB circulations are more pronounced during dry, sunny periods (Planchon et al. 2006). Therefore, the analysis concentrates on the dry seasons (DJF and JJA) to identify LB events during the 6-yr study period from 2017 to 2022. Since not all AWSs were operational throughout the entire period, we limit our analysis for each station to days with more than 80% of wind or temperature data records. Therefore, data availability varies among stations depending on the installation date, with 42 (36) of the 45 stations having more than 60% (80%) subdaily data availability (see Fig. 2 and Table S1 in the online supplemental material). Additionally, the stations are classified relative to their distance from LV as follows: A (<7 km), B (7–20 km), C (21–40 km), D (41–80 km), and E (>80 km) (see Figs. 1 and 2).

2) Satellite images

In addition to ground-based station data, this study incorporates visible satellite imagery from NASA's Earth Observing System Data and Information System (EOSDIS) Worldview platform (NASA EOSDIS Worldview)[1] to identify LBFs during the DJF and JJA seasons over the 2017–22 period. The analysis utilizes visible spectrum channels from the Moderate Resolution Imaging Spectroradiometer (MODIS) aboard NASA's *Terra* and *Aqua* satellites, as well as the Visible Infrared Imaging Radiometer Suite (VIIRS) onboard the *Suomi NPP* and *NOAA-20* satellites. These satellites provide twice-daily overpasses (nominal equatorial overpass times) over the study region at the following local times: 1030 and 2230 for *Terra*-MODIS, 1220 and 0020 for *NOAA-20*/VIIRS, and 1330 and 0130 for both *Aqua*-MODIS and *Suomi NPP*/VIIRS. The thermal band spatial resolution is ~250 m per pixel for MODIS

[1] https://worldview.earthdata.nasa.gov/.

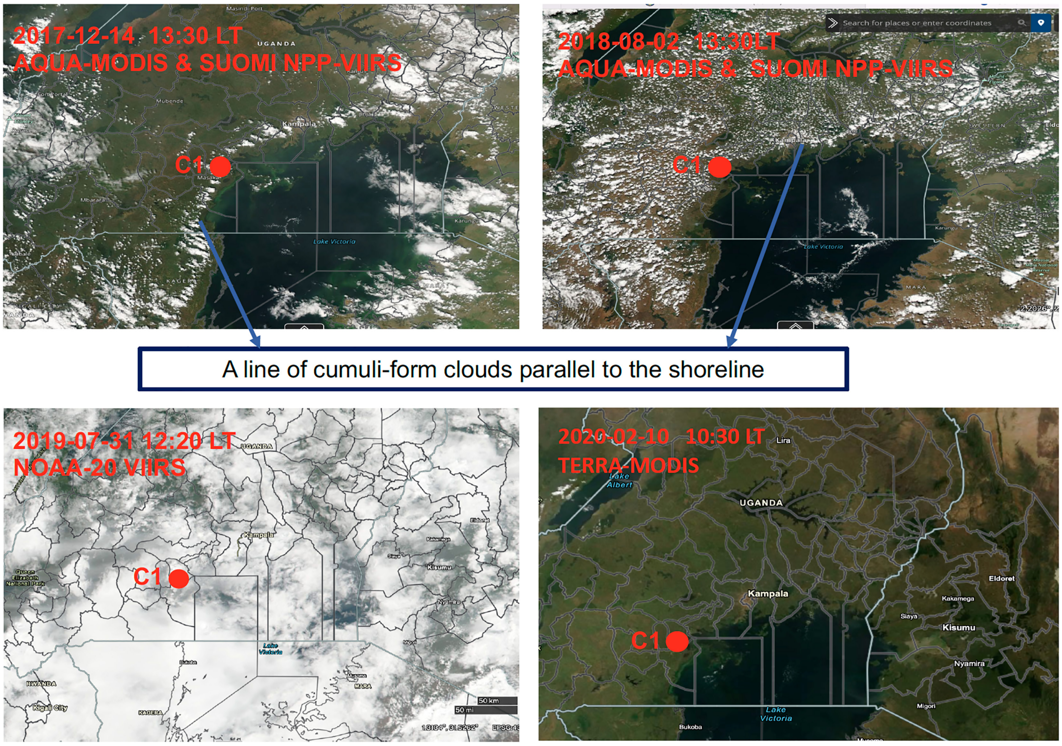

FIG. 3. (top) Examples of the manually identified satellite LB days on which LBFs were visible around LV from NASA EOSDIS Worldview visible spectrum images. A line of cumulus-form clouds aligned parallel to LV's shoreline advecting inland shows the presence of the LBF on these days. (bottom) Examples of satellite non-LB days: a cloudy day and a completely cloud-free day image. The red-shaded circle in all panels indicates the location of Kamenyamigo station (C1), which is also passed by the LBF in the top panel subfigures.

and 375 m per pixel for VIIRS, enabling detailed observation of mesoscale atmospheric features.

3. Methods

a. Sampling potential lake-breeze candidates from satellite images

Using visible spectrum satellite imagery, LBFs are often identified by the presence of cumulus-form cloud lines aligned parallel to the shoreline and moving inland under the influence of LB circulation (Simpson 1994). However, not all LB circulations result in visible cloud lines, particularly in conditions of low atmospheric humidity, when cloud development may be suppressed, rendering the LBF undetectable in visible imagery. Thus, the absence of visible cloud lines does not necessarily indicate the absence of a lake breeze.

To effectively identify LB events in our study area, the northern shores of LV were partitioned into three coastal sectors based on coastline orientation and complexity: western (W: 30°–32°E, 0°–1°S), northwestern (NW: 31°–32°E, 0°–1°N), and northern (N: 32°–34°E, 0°–1.3°N) (Fig. 1). Then, visible spectrum satellite images from NASA EOSDIS Worldview were visually inspected for the dry seasons of DJF and JJA over the period 2017–22. Days such as those shown in Fig. 3, exhibiting clear cloud lines aligned parallel to the coast, were catalogued as LB days, while days with no discernible LB features were recorded as non-LB days in this study. Furthermore, days characterized by (i) strong synoptic disturbances with extensive cloud cover or (ii) entirely cloud-free conditions across the study area were considered as non-LB days following the screening methodology of Planchon et al. (2006) and Damato et al. (2003).

In addition to using linear, coherent cloud bands as the primary indicator of LB activity, the visual inspection also considered other supporting mesoscale cloud structures (e.g., horizontal convective rolls and cloud streets) when their orientation and timing were consistent with expected LB evolution. These combined qualitative indicators formed the basis of the satellite-derived reference dataset. For each of the 1093 dry-season days examined, 2–3 visible spectrum satellite images (depending on overpass times) were reviewed to ensure consistency in identifying LB-related cloud signatures. Of these days, 578 were classified as LB days and 210 as non-LB days. Days for which the satellite scene did not allow for a confident classification were designated as "uncertain" and excluded from the analysis to minimize potential misclassification and to maintain a robust comparison between clear LB and non-LB cases. These resulting LB and non-LB samples serve as the "reference" dataset for validating the LBF detection algorithm for ground-based station data, as described in the next section.

b. Description of the objective OLBDA

1) General overview of the algorithm

The algorithm is developed using key characteristic features of SBF/LBF passage at an observing station, with all its main components described in more detail in the next section. The algorithm begins by checking for onshore winds at a test station, a compulsory flag based on the definition of sea-/lake-breeze circulation that must be satisfied before proceeding to the next step. If this is passed, then it checks for a change in environmental conditions at that station as a result of the marine air mass from the lake replacing the air over land. For example, when a LBF passes over a test station, there is a rapid increase in onshore wind speed usually accompanied by a sharp decrease in temperature and an increase in humidity or dewpoint (Sills et al. 2011; Miller et al. 2003). Finally, the algorithm checks whether the above changes were not a result of cold pools of convective systems. By doing this, the algorithm ensures that all the changes in the measured meteorological parameters are exclusively produced by lake-breeze frontal passages. If all these criteria flags are passed sequentially, then the LBF passage at that station is counted. The complete sequence of procedures employed to automatically identify LBF occurrences at a station is outlined in the OLBDA flowchart (Fig. 4).

2) Detailed description of the algorithm

The OLBDA shown in Fig. 4 processes 15-min instantaneous observations of 2-m temperature, dewpoint, and wind at each station, iterating through the time series and comparing each observation with the one from 15 min earlier to detect 15-min changes. For example, at 0915 LT, the algorithm compares the observations from 0915 LT with those recorded at 0900 LT. Then, it is incremented to 0930 LT and compared with the observations from 0915 LT. This 15-min window was chosen because it was the highest temporal resolution available across all stations and is sufficient to capture changes due to LBF passage.

Like in Hughes and Veron (2018) and Hawbecker and Knievel (2022), we identify LBs by focusing on daytime periods when the coastal land–lake temperature contrast is assumed to be strong. Specifically, the algorithm searching times are limited to 0900–1900 LT during the dry months (i.e., DJF and JJA). The three different criteria employed to detect lake-breeze episodes from station observational data are described in the following.

(i) Wind shift and wind speed increase criteria

Based on the definition of the sea-/lake-breeze circulation, onshore winds are expected (e.g., Azorin-Molina et al. 2011; Hughes and Veron 2018); hence, the algorithm starts by defining an onshore wind direction for each station. That is, for each station, we define the onshore angle range such that it encompasses the extent/shoreline of LV as illustrated in Fig. 5. If the recorded wind direction at this station falls within this range, it is classified as onshore; otherwise, it is classified as offshore.

A potential LBF passage is detected at any given station and time if one of the following wind conditions is met: either there is a rapid shift in wind direction from offshore to onshore (i.e., wind direction reversal) or there is a rapid increase in wind speed in the onshore direction within a 15-min period at the onset of the lake breeze. Owing to the complex shape of LV's shoreline, wind shifts at individual stations are defined relative to the orthogonal of the nearest shoreline.

Although a shift from offshore to onshore often accompanies LBF passage, this is not typical in our study area due to its location and prevailing large-scale synoptic flow, which is predominantly easterly at low levels (northeasterly in DJF and southeasterly in JJA). In such cases, LBF passages can be associated with increases in wind speed driven by a positive land–lake temperature contrast (Azorin-Molina et al. 2011). Consequently, our algorithm is designed to detect LBFs without explicitly requiring wind reversal, but onshore wind remains a mandatory condition to exclude signals from other phenomena such as synoptic fronts (Borne et al. 1998) and must be satisfied before the algorithm proceeds to identify an LBF passage.

(ii) Temperature criterion

Once the wind direction and speed criteria are met, the data are tested for a drop in air temperature or an increase in dewpoint temperature, which are often associated with the influx of cooler moist air coming from the lake.

Given the variability in temperature drops and dewpoint increases across stations (Fig. 1), applying a single fixed threshold was not feasible. For example, Fig. 6a illustrates that a fixed 0.5°C temperature drop (black dashed line) in 15 min would miss many LBF passages at stations A1, A3, A4, B5, B7, and D9, since this value exceeds the interquartile range at these stations. Similarly, Fig. 6b shows that a fixed 0.5°C dewpoint increase would underestimate LBF occurrences at most stations.

As a result, percentile-based thresholds for temperature and dewpoint criteria are applied to account for regional variabilities. Here, the lowest (highest) 30% of the air (dewpoint) temperature decreases (increases) in the dry seasons are used, making temperature change thresholds station dependent. These percentile thresholds stem from a performance test of OLBDA that is presented later in section 4b.

(iii) Exclusion of cold pool passages

A day is not counted as a lake-breeze day if there is significant precipitation within 3 h prior to the potential LBF passage detection, including the time of arrival at the station. This filter was introduced to minimize misclassification, since precipitation-related convective cold pools can generate temperature, dewpoint, and wind changes similar to those associated with LBF passages. Accordingly, this algorithm requires that in the case of any precipitation at a station in the preceding 3-h period inclusive of arrival time, it should not exceed 0.1 mm prior to the LBF passage. The filter therefore removes any candidate LBF event coinciding with antecedent precipitation at the station above this threshold. By contrast, cases in which precipitation develops after LBF detection are retained.

If in any 15-min interval, all the three specified criteria are satisfied at a given station, the entire day is classified as an LB

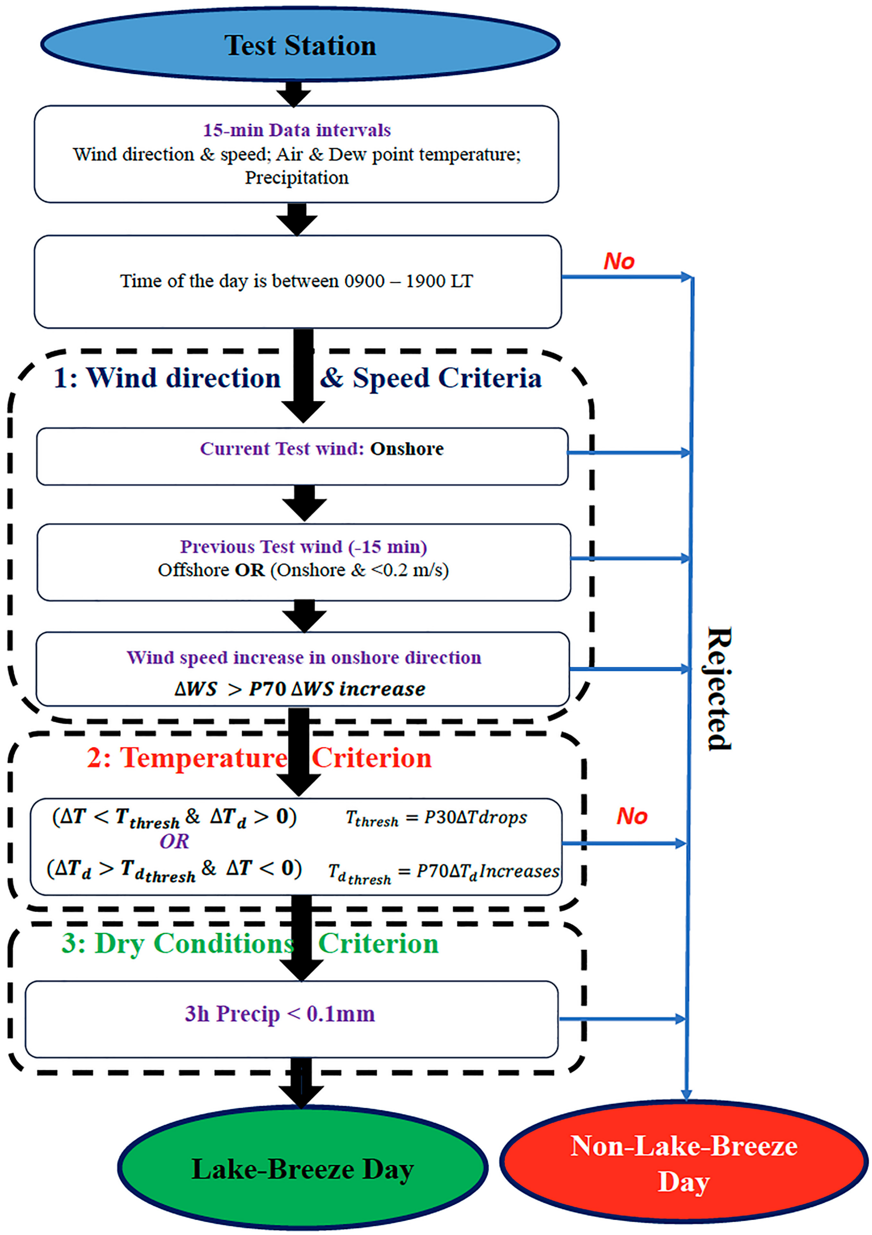

FIG. 4. Flow diagram showing the three different criteria used by OLBDA to objectively detect LBF passage at a station using meteorological data of temperature, dewpoint, wind, and precipitation. If the station time series on that day meets all the three criteria checks, then the day is classified as a lake-breeze day; otherwise, it is classified as a nonlake breeze day. The ΔT, ΔT_d, and ΔWS refer to 15-min changes in temperature, dewpoint, and wind speed, respectively, while P30 and P70 refer to the 30th and 70th percentile values of these changes.

day for that station. The timing of the LBF passage can be used to examine the expected changes in the meteorological variables resulting from the front's passage over a particular station as shown later in the results section.

c. *Verification of OLBDA-detected lake-breeze days*

To test performance, the OLBDA-detected LB days at a given station were compared with the manually identified satellite LB and non-LB days ("reference dataset") in the same geographical area. The number of identified lake-breeze days in both OLBDA and satellite gives the hits (H), while the number of OLBDA-detected LB days common in the satellite non-LB days gives the false alarms (F). The number of satellite LB days that were not detected by the OLBDA gives the misses (M), while the number of non-LB days in both OLBDA and satellite gives correct negatives (N). From this,

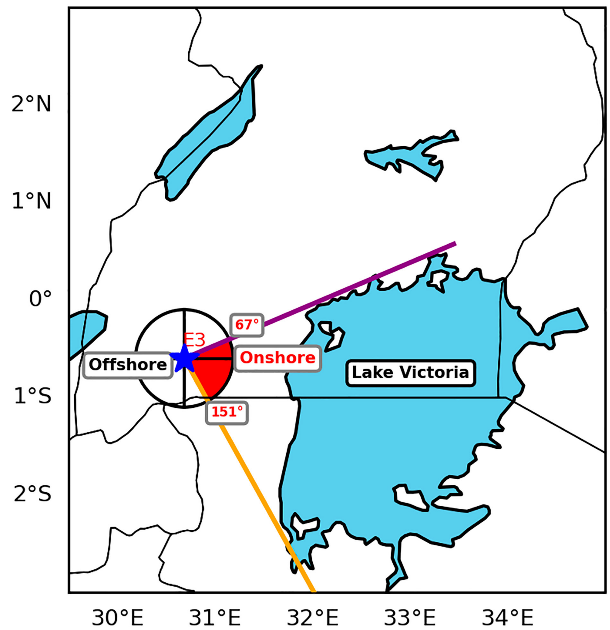

FIG. 5. An illustration of how onshore angle ranges were determined at any station. The onshore angle range (red shading) is defined based on the minimum and maximum radial lines from the point of interest toward LV in a clockwise sense and intersecting with it. In this example, the blue star represents the station of interest (Mbarara; E3) for which the onshore minimum (67°; purple line) and maximum (151°; orange line) angles are determined. If the wind direction at this station lies between these two angle values, then it is characterized as an onshore wind; otherwise, it is offshore (no shading).

a 2 × 2 contingency table (Table 1) was formed, and the evaluation of the OLBDA was carried out using the performance metrics, namely, probability of detection (POD), probability of false alarm (POFA), success ratio (SR), critical success index (CSI), bias in detection (BID), accuracy (ACC), and Heidke skill score (HSS). The description and calculation of each statistic are summarized in Table 2.

d. Deriving lake-breeze characteristics

After the LBF passage is detected at a station, that day is classified as a lake-breeze day at that station. Then, LBF occurrences are analyzed for LB frequency and onset (arrival) time statistics. Additionally, the LBF occurrences are analyzed for diurnal, seasonal, and interannual variability. To assess the meteorological conditions surrounding the passage of the LBF, each LB day is aligned such that time, t_0 ($t = 0$), corresponds to the LBF's arrival time. This alignment enables a comparative analysis of atmospheric variables within a 3-h window before and after the event, offering insights into the directional persistence of the LB and associated meteorological changes. Furthermore, inland penetration characteristics such as LBF speed and depth are investigated using transects in different directions. For example, when the LBF moves through two of the stations along a transect, the difference in the frontal arrival time is used to calculate the LBF speed between those two stations. Finally, a snapshot climatology of lake-breeze characteristics is developed.

4. Results

a. Example of lake-breeze front passage detected by the OLBDA

This section presents an example of the LBF passage detected by OLBDA on 14 December 2017 at Kamenyamigo station (C1), located ~28 km from LV along the western coast. The algorithm detected the LBF passage at approximately 1600 LT, coinciding with notable changes in atmospheric variables (Fig. 7). Specifically, air temperature dropped by 1.4° and 1.3°C over two consecutive 15-min intervals, while dewpoint temperature increased by 4° and 2°C, respectively. These abrupt changes exceeded the thresholds defined by the lowest (highest) 30% of the air (dewpoint) temperature decreases (increases) at Kamenyamigo by more than 0.8°C (1.6°C). Concurrently, wind direction shifted from northerly (offshore) to easterly (onshore), accompanied by a marked increase in wind speed. These changes are characteristic of the LBF passage. The passage time (i.e., 1600 LT) is defined as the moment when a sharp temperature drop and a simultaneous rise in humidity are observed, marking the arrival of the thermodynamic front. This OLBDA-detected LB day was also confirmed by the satellite image in Fig. 3 (top left).

b. Sensitivity test: Identification of the best configuration

To optimize the algorithm, multiple configuration setups were tested to identify the most effective threshold combination for detecting LBF passages at near-coastal stations. We only selected coastal stations based on the certainty that the LBF passed them as visually seen from the satellite images in Fig. 3. The algorithm operates on absolute 15-min changes in air temperature, dewpoint, and wind speed rather than percentage changes. Accordingly, all percentile thresholds used in the sensitivity analysis were derived from the empirical distributions of these absolute changes and are independent of the baseline meteorological conditions at each station. This approach ensures that the thresholds represent characteristic magnitudes of short-term variability rather than proportional departures from the background state.

The algorithm's sensitivity was evaluated by systematically varying percentile thresholds for air temperature drop, dewpoint, and wind speed increase. In this framework, each percentile corresponds to a defined portion of the observed distribution at each station (e.g., a combination of P30, P70, and P70 means the lowest 30% of temperature drops, the highest 70% of dewpoint increases, and the highest 70% of wind speed increases), allowing us to evaluate how increasingly stringent or permissive criteria affect detection performance. The resulting impacts on POD, POFA, SR, CSI, and BID are summarized in the performance diagram in Fig. 8.

A total of 58 configuration setups were assessed, including two configurations with fixed thresholds for temperature, dewpoint, and wind speed changes. Each configuration yielded varying LBF detection counts, confirming the algorithm's sensitivity

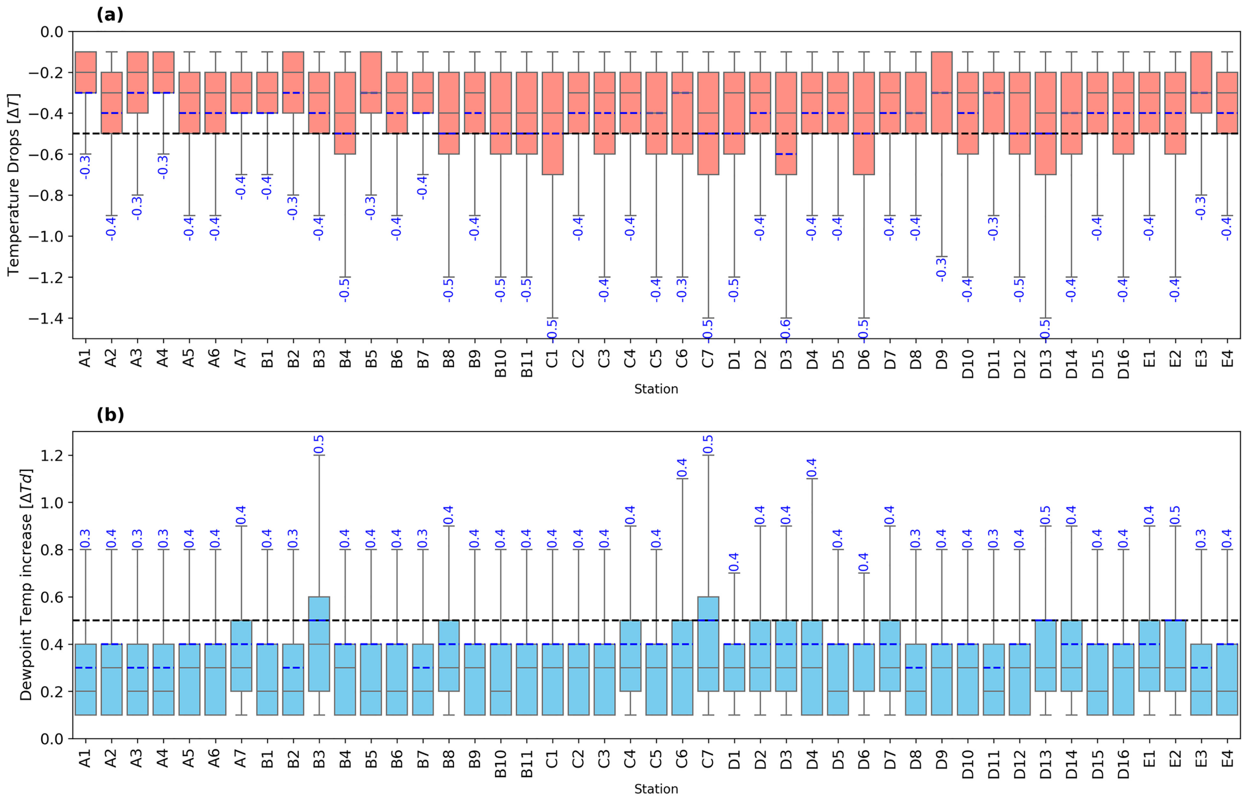

FIG. 6. Box-and-whisker plot showing the distribution of 15-min (a) temperature drops and (b) dewpoint increases at every station within the study area during the dry seasons of DJF and JJA and within 0900–1900 LT. On each box, the black central mark is the median; the top and bottom of the box are the upper and lower quartiles, respectively. The black-dashed line exemplarily represents the −0.5°C (0.5°C) temperature (dewpoint) change, respectively, across the different stations. The blue-dashed line in each box indicates the percentile-based threshold value (also annotated at the top of each whisker) for each station.

to threshold values. To identify the most effective setup, performance metrics were calculated for the identified LBF events with each configuration and then averaged across stations. The station ensemble mean position of each configuration was then plotted on the performance diagram for easy comparison. As shown in Fig. 8, the "P40–P60_ΔWS > 0" configuration had the highest POD but also the highest POFA and BID, indicating overdetection, while the "$\Delta T\_\Delta T_d$ = 0.5_ΔWS = 0.2" configuration showed the highest SR (0.81) but a lower POD (0.57) and CSI (0.50). Conversely, the "P40–P60–P60" was unbiased (BID = 1) but had a lower SR (0.75). The most balanced configuration for identifying LBFs was "P30–P70–P70," with POD = 0.74, SR = 0.79, CSI = 0.62, and BID = 0.95. Thus, the "P30–P70–P70" configuration (see highlighted marker in Fig. 8), representing the lowest 30% air temperature drops and highest 70% dewpoint and wind speed increases in the dry seasons, was adopted as the optimal threshold for these parameters in the algorithm.

TABLE 1. A 2 × 2 contingency table for comparing algorithm-detected LB days and satellite-identified LB and non-LB days.

	Satellite LB day	Satellite non-LB day
OLBDA LB day	Hit (*H*)	False alarm (*F*)
OLBDA non-LB day	Miss (*M*)	Correct negative (*N*)

c. Station-based performance evaluation

To evaluate performance, OLBDA-detected LB days obtained using the most suitable configuration from section 4b are compared with the manually identified satellite lake-breeze days during the study period.

The OLBDA algorithm demonstrates robust performance in detecting LB events, particularly at coastal stations. It achieves a high POD (POD > 0.7), low false alarm ratio (POFA = 0.2), and good overall accuracy of 0.76, although it slightly underestimates LB frequency (BID = 0.95) (see Fig. 8). The spatial distribution of performance metrics is shown in Fig. 9. Figure 9a shows that POD values in the western sector and within 20 km of the shoreline are higher than 0.6, while beyond 70 km, they are less than 0.40. This indicates that the algorithm correctly captures the majority of the LB days identified by the satellite, especially near the coast, likely because the changes in wind and temperature are stronger. About 93% of the stations have POFA values below 0.25, with an average value of 0.19 (Fig. 9b), implying that 19% of detected LB events at these stations are false alarms. The CSI, SR, and ACC patterns (Figs. 9c–e) align closely with those of POD, indicating

TABLE 2. A summary of the different performance metrics used in this study to validate the algorithm. The terms H, F, M, and N denote hits, false alarms, misses, and correct negatives, respectively. The range and the best score of each statistic are given in the first column in square brackets and the bold numbers, respectively.

Statistic	Formula	Description
POD; [0, 1], **1**	$\mathrm{POD} = \frac{H}{H+M}$	Quantifies the ability of the OLBDA to correctly detect LB days
POFA; [0, 1], **0**	$\mathrm{POFA} = \frac{F}{H+F}$	Proportion of OLBDA-detected lake-breeze days that were non-LB days in the satellite
SR; [0, 1], **1**	$\mathrm{SR} = \frac{H}{H+F}$	Compares the number of correctly detected LB days with the total number of OLBDA-detected LB days
CSI; [0, 1], **1**	$\mathrm{CSI} = \frac{H}{H+F+M}$	Ratio of all LB days detected and observed which are correctly detected
BID; [−∞, +∞], **1**	$\mathrm{BID} = \frac{H+F}{H+M}$	Assesses whether the OLBDA overestimates or underestimates LB-day frequency
ACC; [0, 1], **1**	$\mathrm{ACC} = \frac{H+N}{H+N+F+M}$	Quantifies the ability of the OLBDA to correctly detect LB and non-LB days
HSS; [−∞, 1], **1**	$\mathrm{HSS} = \frac{2(HN-FM)}{(H+M)(M+N)+(H+F)(F+N)}$	Accesses the skill of the OLBDA compared to random chance

consistent detection reliability. The majority of stations exhibit CSI > 0.4 (73%), SR > 0.7 (98%), and ACC > 0.6 (93%), with coastal stations having the highest values across all three metrics. The mean CSI value of 0.49 across all stations implies that the algorithm correctly detects nearly half of the LB events (observed and/or detected). As with other metrics, the HSS in Fig. 9f highlights greater detection skill near the coast, diminishing inland. With a mean HSS value of 0.37, OLBDA demonstrates a higher ability to detect LBF passages compared to random chance at most stations. Overall, OLBDA effectively captures most satellite-identified LB days, underscoring its high suitability for LB detection, particularly along the coast. The diminishing detection skill further inland is related to the fact that not all LBFs actually reach the inland stations as some may weaken or stagnate while moving inland due to the weak onshore flow, potentially leading to an overestimation in the number of misses at these stations.

d. Application of algorithm

After evaluating the algorithm's performance, the algorithm was applied to extract several LB features as discussed in the following subsections.

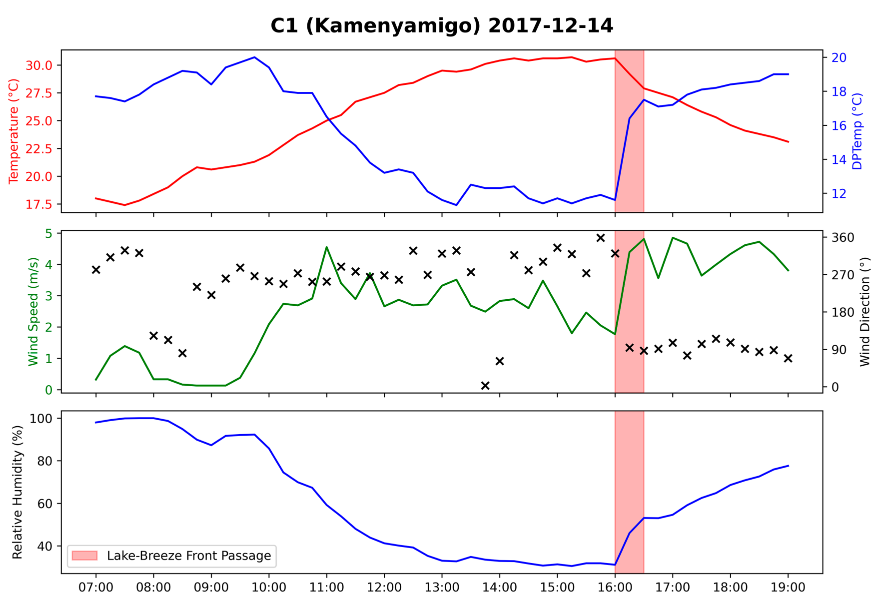

FIG. 7. Case study from 14 Dec 2017 portraying the meteorological effects of a lake-breeze frontal passage at station C1 (Kamenyamigo) as detected by the OLBDA. The (top) temperature, (middle) wind speed and direction, and (bottom) relative humidity before and after LBF passage are shown. The red shading indicates LBF passage. This same day was captured by the satellite images (see Fig. 3; top left).

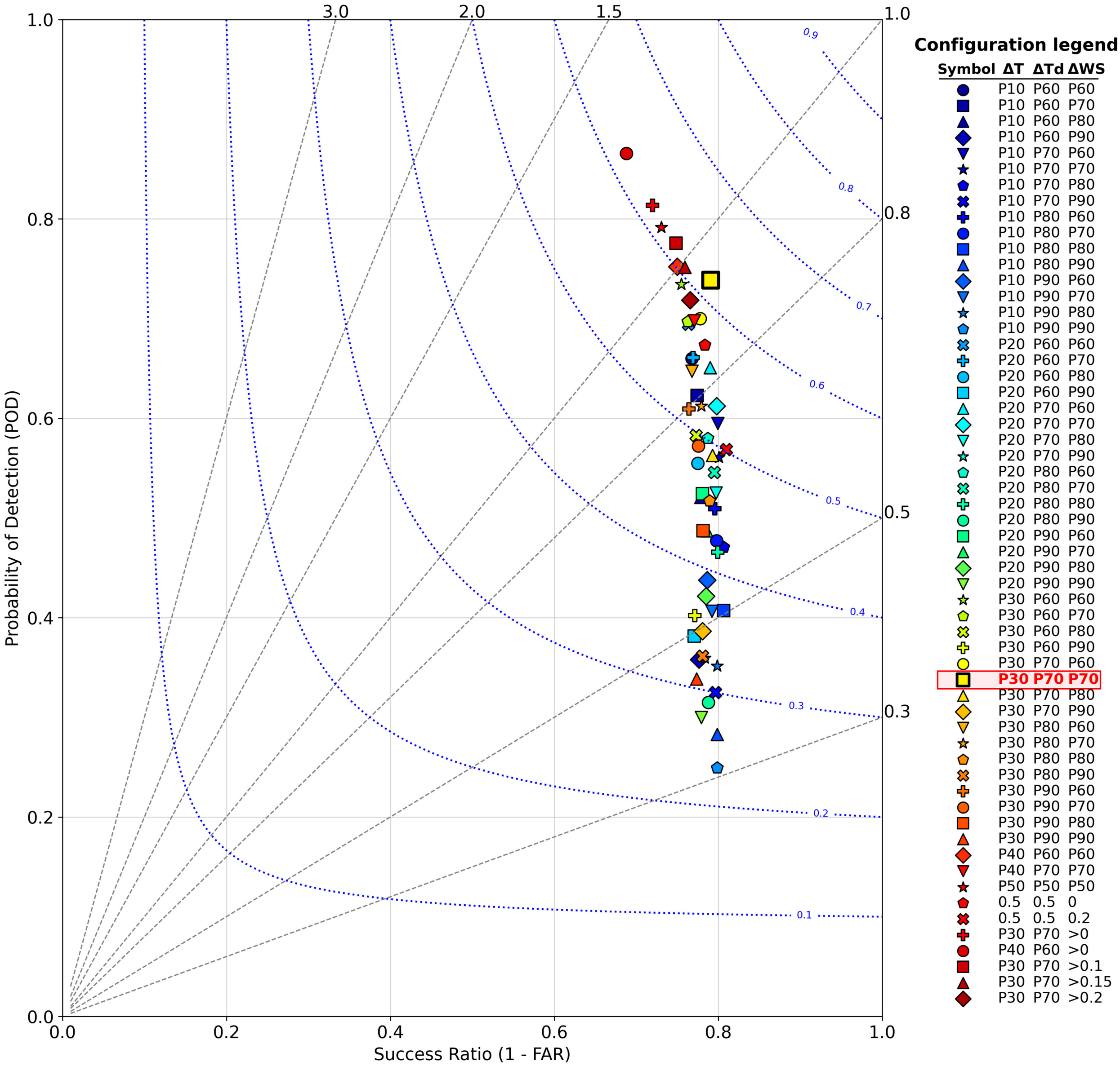

FIG. 8. Performance diagram for near-coastal stations showing the POD (horizontal lines), SR (vertical lines), CSI (blue dotted lines), and bias (BID; gray dashed lines). The diagram summarizes sensitivity tests based on varying temperature and wind thresholds used in algorithm tuning. In the legend, the leading "P" denotes percentiles of air temperature decrease (ΔT), dewpoint increase (ΔT_d), and wind speed increase (ΔWS) applied in the different configurations. Markers indicate the ensemble mean position for each sensitivity test. The red, bolded configuration (P30–P70–P70), highlighted with a black-edged yellow square marker, represents the eventual configuration used.

1) OBSERVED LAKE-BREEZE FREQUENCY AND VARIABILITY

(i) *Overall observed frequency*

Using results from the algorithm, a day is considered as a LB day in this study if OLBDA detects LBF passage in at least three arbitrary coastal stations on that day. Based on this definition, a total of 524 LB days were identified out of 1093 days in DJF and JJA considered (Table 3), representing 48% (i.e., one LB event every 2.1 days). Of these LBs, 428 (81.7%) were detected on the western sector and 476 (90.8%) on the northern sector of LV. The variation in frequency is partly due to the availability and location of coastal stations used on either side of the lake. For instance, the closest station to the coast on the western side is 27 km away, while on the northern side, it is only 0.2 km (see Fig. 1, Table S1). Consequently, the observed LB frequency on the western side is likely underestimated, as weaker LBs that cannot penetrate far enough inland go

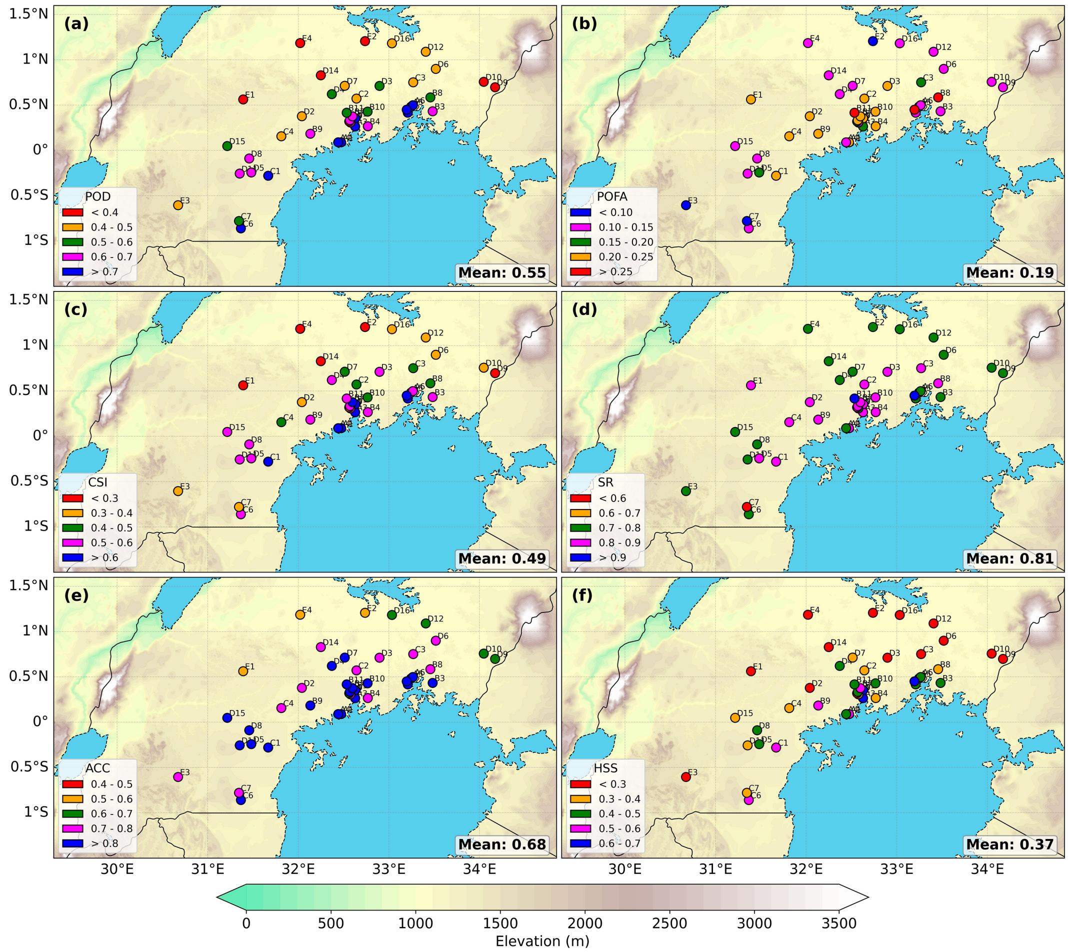

FIG. 9. Spatial distribution of (a) POD, (b) POFA, (c) CSI, (d) SR, (e) ACC, and (f) HSS for the algorithm's performance at different stations in the study area. The mean value for each metric is indicated in the bottom-right corner of each subpanel. The background shading shows the elevation from GLOBE (Hastings et al. 1999).

undetected. Table 3 also reveals that the number of LB days per year is not evenly distributed, with 2021 (2018) having the most (least) LB days of 111 (58), respectively, out of the 182 available days. This indicates interannual variability in the frequency of LB occurrence.

Figure 10 shows the spatial distribution of LB days during the dry months (December–February and June–August) throughout the entire study period. During daylight hours (0900–1900 LT), LBF passages are observed at most stations on 12%–54% of the days (Fig. 10; Table S2). Furthermore, Fig. 10 and Table S2 reveal substantial spatiotemporal variability in the frequency of LB days across the entire study region. For instance, the proportion of detected LB days varies by sector: 4%–54% in the N, 3%–33% in the NW, and 10%–44% in the W sectors. Like seen in section 4c, station proximity to the coastline plays a significant role, with coastal stations consistently recording higher LB-day frequencies (Fig. 10). As explained previously, not all LBFs propagate deeply inland. This results in fewer detections inland as most LBFs dissipate before reaching inland stations. Consequently, the misses are potentially overestimated at these stations.

TABLE 3. Total number of LB days detected in DJF and JJA on the western coast (W) and northern coast (N).

Year	No. of days (DJF–JJA)	Total LB days	LB days (W)	LB days (N)
2017	182	72	53	72
2018	182	58	48	54
2019	182	83	63	77
2020	183	99	82	85
2021	182	111	93	98
2022	182	101	89	90
Total	1093	524	428	476

(ii) A case of A1 (Entebbe WDD) and C1 (Kamenyamigo) stations

Figure 11 demonstrates distinct differences in the frequency and diurnal timing of LB occurrences at two stations close to the coast with the most complete dataset (2017–22): Entebbe WDD (A1, N) and Kamenyamigo (C1, W). As expected, A1,

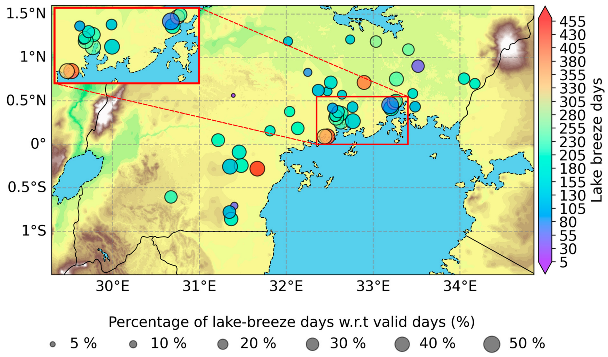

FIG. 10. Spatial distribution of lake-breeze days at each station (see Fig. 1) for the period 2017–22 during the dry months of DJF and JJA. The color represents the number of lake-breeze days recorded at each station, while the size of the circle represents the percentage of lake-breeze days relative to the total number of valid days at that station.

located just 0.2 km from the coast, experiences lake-breeze conditions earlier in the day than C1, which lies farther inland (Fig. 11a). Typically, LBFs arrive between 0900 and 1900 LT, peaking at 1200 LT for A1 and 1500 LT for C1, indicating a systematic shift with increasing distance from the coastline. This pattern underscores the strong influence of coastal proximity on LBF timing, consistent with findings by Odongo et al. (2022), who used ERA5 data to study lake breezes at these stations.

Figure 11b reveals that LB occurrences peak in January and August and are lowest in June at both stations. The highest LB occurrences in January and August can be attributed to being the hottest months of the year in the area, whereas the lowest occurrences in June are partly due to the transition from the long March–May rain season. Comparing the two dry seasons, DJF records more LBs than JJA, with A1 and C1 registering 226 and 255 events in DJF, against 188 and 197 in JJA, respectively. This is supported by an auxiliary temperature analysis (not shown) which shows slightly higher temperature gradients in DJF than JJA on average.

Frequency of lake breezes at any given station also varies interannually. Table 4 and Fig. 11c demonstrate the variability for A1 and C1 stations. At these stations, lake breezes were detected on 35%–52% and 26%–59% of dry season days depending on the year for A1 and C1, respectively (Table 4). The annual LBF frequency at these stations shows a year-to-year variability, typical of what is seen across the study region. These results corroborate with findings in the previous subsection.

2) OBSERVED LAKE-BREEZE CHARACTERISTICS

(i) Mean observed conditions before and after LBF passage

To illustrate the spatial variation in the atmospheric conditions introduced as the LBF propagates through different directions, the changes in the observed meteorological variables 3 h before and after the detected LBF passage are averaged and aligned with respect to the frontal passage as presented in Fig. 12. On average, the mean air temperature sharply drops by over 0.75°C in response to the passing of the front and continues to decrease steadily for the next 3 h on all sides of the lake after the LBF passage (Fig. 12a). This is probably due to the late arrival of the front mostly in late afternoon coinciding with a decrease in incoming solar radiation as suggested by Hughes and Veron (2018). Also, the small temperature change is most likely related to the weak temperature gradient between the lake and the land. Notably, the temperature drop remains consistent in western and northwestern sectors even after the front passage. The mean dewpoint shows a similar trend across all sectors, increasing by over 0.7°C ahead of the frontal passage and continues to increase briefly after the passage, peaking within 15 min (Fig. 12b). Thereafter, the dewpoint starts to drop slightly in all sectors. The northern sector shows the greatest increase (~0.9°C), while the western sector records the lowest (0.7°C), indicating a westward reduction in moisture influx during the LBF passage. The slight drop in dewpoint after the peak may be attributed to the mixing of incoming cooler marine air with warmer air over land within the convective internal boundary layer.

On the other hand, the mean relative humidity exhibits a reverse pattern to that of mean temperature, increasing by over 5% ahead of the LBF passage and even after the frontal passage for all sectors (Fig. 12c). Like for dewpoint, the greatest increase

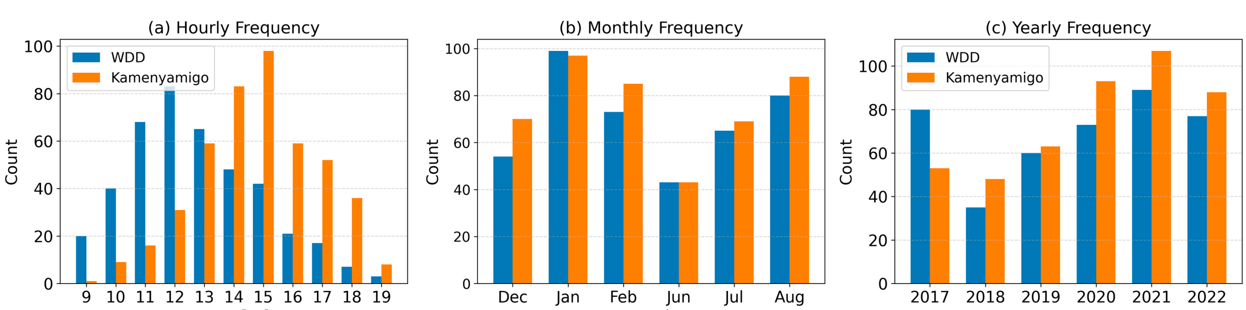

FIG. 11. Bar graphs showing the occurrence of lake-breeze events detected using the algorithm at Entebbe WDD (A1; *N*) and Kamenyamigo (C1; *W*) stations during the dry seasons (DJF and JJA) between 2017 and 2022 in terms of the number of detected events by (a) hour, (b) month, and (c) year. These stations are the closest to the coastline in each sector, with the most complete dataset during the period 2017–22.

TABLE 4. LBF occurrences at Entebbe WDD (A1, N) and Kamenyamigo (C1, W) stations showing interannual variability.

	Entebbe WDD (A1)			Kamenyamigo (C1)		
Year	DJF–JJA valid days	LB days	LB days percentage (%)	DJF–JJA valid days	LB days	LB days percentage (%)
2017	170	80	47.1	182	53	29.1
2018	84	35	41.7	182	48	26.4
2019	172	60	34.9	182	63	34.6
2020	172	73	42.4	183	93	50.8
2021	172	89	51.7	182	107	58.8
2022	173	77	44.5	182	88	48.4

in relative humidity is experienced on the northern sector, while the lowest increase occurs on western side of the lake.

Last, the winds weaken after the frontal passage in all directions except for the northern sector where they remain steady for 15 min before decreasing (Fig. 12d). However, during the frontal passage, wind speed increases sharply in all sectors with a rise of over 0.6 m s^{-1} within 15 min, with western (northwestern) sector showing the greatest (least) increase of 0.85 m s^{-1} (0.65 m s^{-1}).

(ii) LBF arrival times

To assess the influence of coastal proximity on LBF arrival time characteristics, stations were clustered into five groups based on their relative distance from the coastline and their coastal sector (see Fig. 1). Figure 13 presents the spatiotemporal LBF characteristics across these groups. Lake-breeze conditions occur earlier in the day, starting at 0900 LT for stations within 40 km across all sectors (Figs. 13a–c). The median LBF arrival time for stations within 7 km from coast coincides with the peak arrival time of 1400 LT (Fig. 13a). For stations 7–20 km inland, both median and peak arrival times shift to 1500 LT in all sectors (Fig. 13b). This timing remains consistent for the 21–40-km group, except in the NW sector where the peak shifts to 1600 LT (Fig. 13c). In the 41–80-km range (Fig. 13d), the median arrival time is 1500 LT in W and NW sectors and 1600 LT for N, indicating a clockwise delay pattern. However, the peak arrival time in this group is 1600 LT across all sectors.

For stations beyond 80 km, both the median and peak arrival times are further delayed to 1600 LT in the N and NW sectors and 1700 LT in the W (Fig. 13e). This marks a drastic 2-h delay in median arrival time between the 41–80 and >80 km groups in the W sector, with the peak also delayed by 1 h. Notably, no LBFs are detected before 1100 LT in any sector for stations beyond 40 km. Overall, LBFs occur from early afternoon to

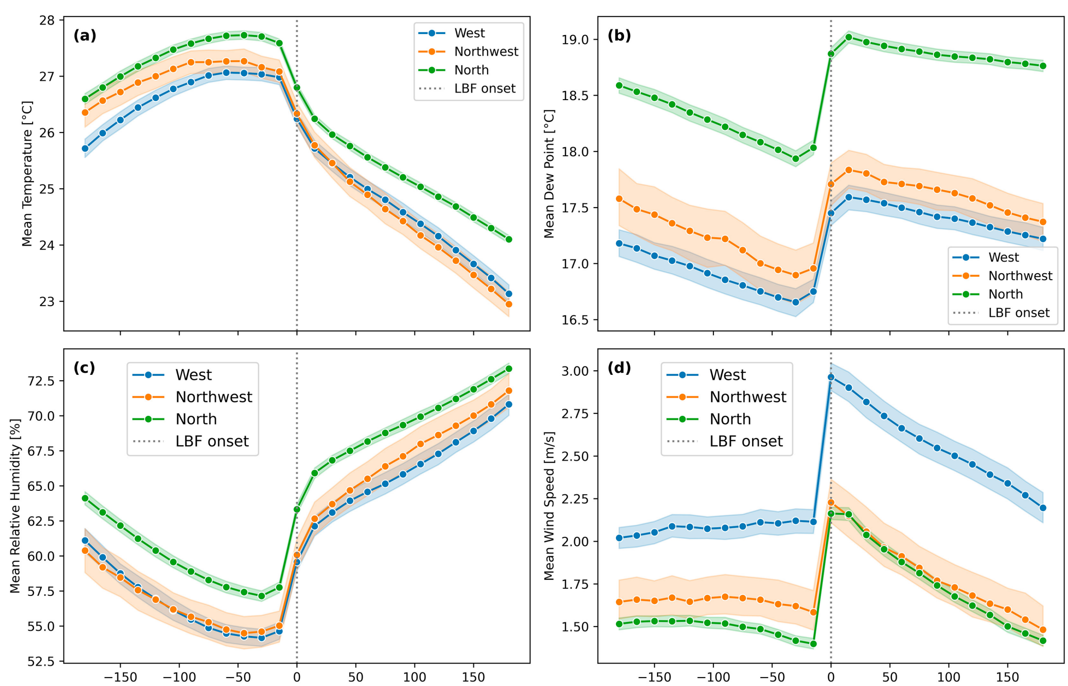

FIG. 12. Mean observed atmospheric conditions before and after LBF passage on the W (blue), NW (orange), and N (green) sides of the lake, for (a) mean temperature, (b) mean dewpoint, (c) mean relative humidity, and (d) mean wind speed. The vertical dotted gray line indicates the first time step that fulfilled the LBF criteria, t_0. The shading indicates the 95% confidence interval.

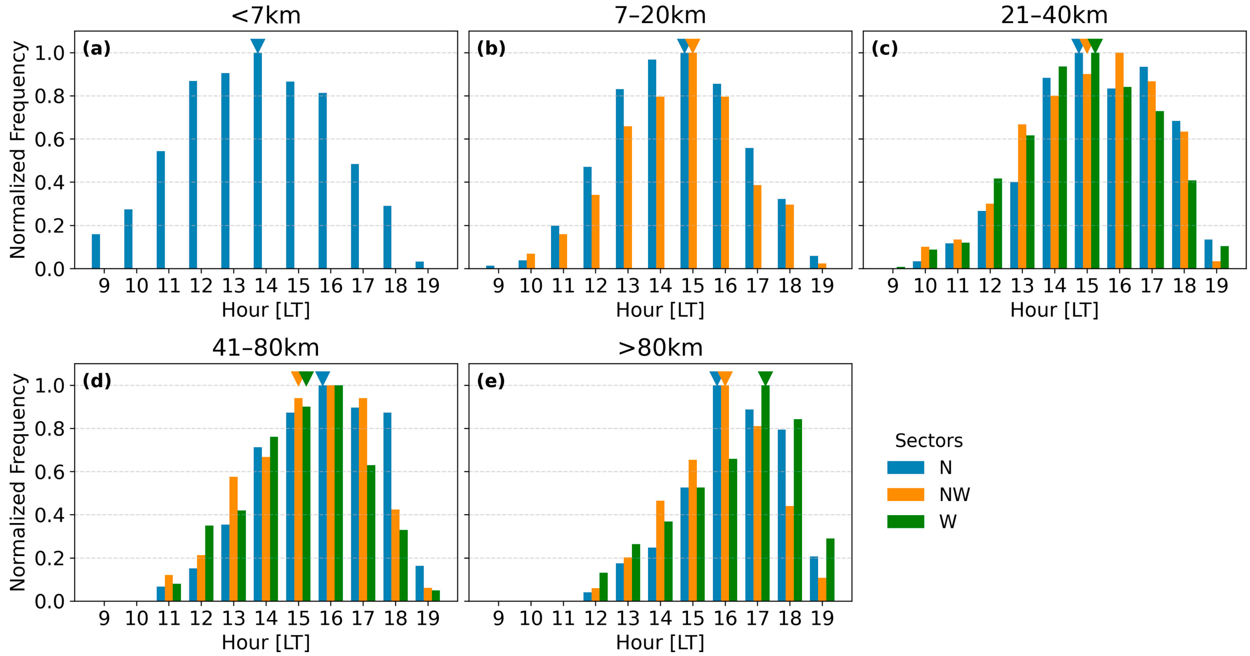

FIG. 13. Bar graphs showing the arrival time of LBFs initially detected at different station classes from the coast: (a) A (<7 km), (b) B (7–20 km), (c) C (21–40 km), (d) D (41–80 km), and (e) E (>80 km) in the three different coastal sectors: N (blue), NW (orange), and W (green). The triangle marker on top of the bars indicated the median arrival time. Note: The hour bin plotted here contains all LBF passages in that hour (e.g., 1000 LT contains all passages between 1000 and 1059 LT).

evening in all sectors, peaking between 1400 and 1500 LT within 40 km of the coast and between 1600 and 1700 LT beyond 80 km. These findings align with those of Datta (1981), who observed maximum LBF strength at 1500 LT using coastal station observations. Furthermore, these results support the strong influence of coastal proximity on LBF timing.

(iii) LBF propagation characteristics and climatology

To assess LBF propagation and develop its climatology over the northern and western shores of LV, station data along seven transects (T1–T7) in three coastal sectors were analyzed. Isochrones of mean LBF arrival times (Fig. 14) interpolated using cubic polynomial method were used to visualize spatiotemporal inland propagation of the front, with wider spacing indicating faster movement and closer spacing reflecting slower progression. Propagation speed along each transect was estimated using time differences between LBF arrivals at successive stations, representing a relative forward propagation speed. In estimating propagation speed, we explicitly assumed that the LBF travels along a straight-line path between station pairs, consistent with previous station-based tracking methods (e.g., Hughes and Veron 2018). For each successive station pair, the propagation speed was calculated from the interstation distance and the difference in detected arrival times. When multiple station pairs were available, the transect-scale propagation speed was computed from the total distance and travel time. Although this approach provides a practical estimate of LBF propagation, the resulting speeds should be interpreted in light of inherent uncertainties due to the straight-line assumption, interstation spacing, and the potential curvature or spatial heterogeneity of the front.

The analysis presented in Fig. 14 reveals that coastal stations typically experience LBFs between 1300 and 1400 LT, while far inland stations such as E4 (~132 km from the shoreline) record arrivals between 1700 and 1730 LT. Most stations (75%) register mean arrival times between 1400 and 1600 LT, with cessation occurring around 1730 LT. The relatively late onset at coastal stations suggests a weak initial thermal contrast between lake and land, which intensifies in the afternoon after substantial solar heating. These patterns indicate steady inland propagation of the front with the timing and inland extent being controlled by regional climatology and modified by local topography, consistent with previous findings (e.g., Woodhams et al. 2019). The maximum inland extent of ~132 km confirms the findings of Woodhams et al. (2019), who reported propagation up to ~240 km during the dry season.

LBF propagation speeds vary by sector: In the western sector, speeds along transects T1 and T2 averaged ~8 m s^{-1} northwestward; in the northwestern sector, speeds range from 5.2 to 7.6 m s^{-1} for transects T3 and T4, averaging 6.5 m s^{-1}; and in the northern sector, frontal speeds along T5, T6, and T7 average 5.8 m s^{-1} northward. These propagation speeds are consistent with Woodhams et al. (2019) and indicate that LBFs propagate fastest westward and slowest northward of the lake. This directional variation suggests a clockwise decrease in inland speed from west to east, likely driven by alignment with prevailing easterly winds (Fig. S1), as supported by Baker et al. (2001). Additionally, although not shown here, LBFs tend to move slowly within the first few kilometers from

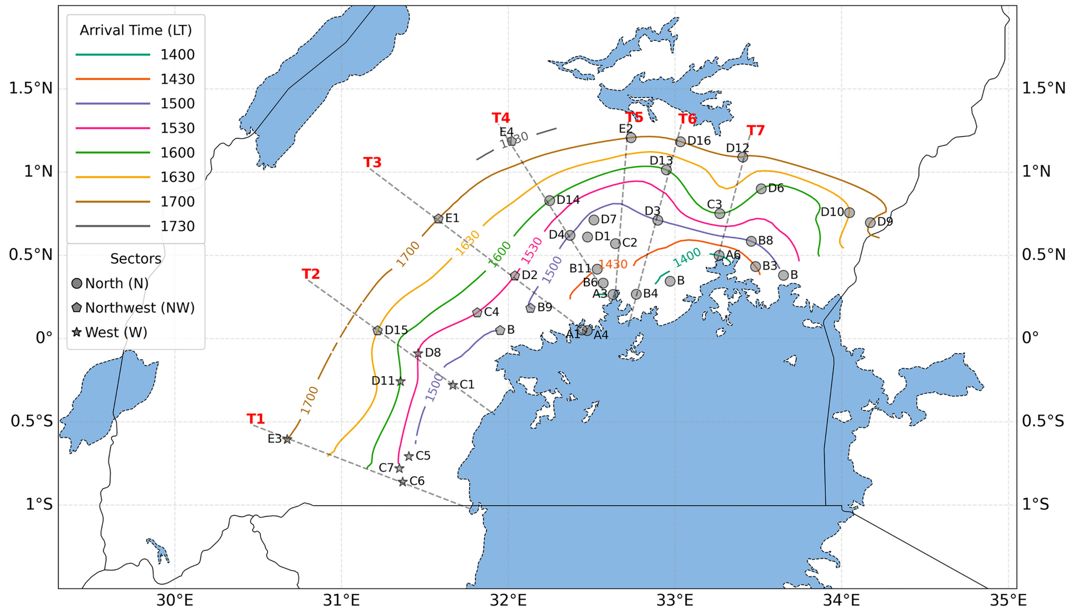

FIG. 14. Spatiotemporal evolution of the LBF being shown by the 30-min isochrones of LBF mean arrival times across stations along the northern and western parts of LV. The dashed gray lines labeled in red boldface (T1–T7) represent transects in different sectors of the lake.

the shoreline before accelerating further inland. This is likely due to increased land friction and urban effects from coastal cities as observed by other studies (e.g., Thompson et al. 2007).

5. Summary and conclusions

Using an unprecedented dense network of AWS, we developed and tested a novel observation-based lake–land-breeze detection algorithm (OLBDA) and inferred climatological LLB characteristics for 2017–22. The OLBDA analyses 15-min temperature, wind speed and direction, and precipitation to objectively identify and detect LBF passages over a range of stations across LVB. It employs three sequential detection criteria: (i) wind-based criterion (wind shift and speed increase), (ii) temperature-based criterion (air temperature drop and dewpoint increase), and (iii) dry-condition criterion that filters out cold-pool passages. Detection is based on station-specific percentile thresholds, defined using the lowest (highest) 30% of temperature (dewpoint and wind speed) decreases (increases), to ensure sensitivity to the subtle signals typical of LBFs in this region. A day is classified as an LB day based on the first daytime LBF passage at a station. Verification against manually identified satellite-based LB and non-LB days shows that OLBDA reliably captures LBF events, especially at coastal stations, demonstrating high detection probability, low false alarm rates, and good overall accuracy. These results confirm that the algorithm effectively detects the small temperature, humidity, and wind speed changes associated with LBFs over LVB.

Applying the OLBDA to all the 45 stations in the study area and analyzing all detected lake-breeze days to determine the LBF characteristics over the northern edge of Lake Victoria in Uganda revealed the following key results:

1) Nearly half (48%) of all DJF and JJA days during 2017–22 featured an LB event (524 of 1093 days), implying one LB event about every 2 days.
2) LBF passages occur on 12%–54% of dry-season days (DJF and JJA) between 0900 and 1900 LT across most stations, with slightly more frequencies in DJF season due to slightly higher temperature gradients. The LB occurrences also exhibit interannual variability in frequency.
3) Station proximity to the LV shoreline significantly influences LBF frequency, with coastal stations consistently recording more events than inland stations. This is partly because LBFs may dissipate before reaching distant stations, leading to potential underestimation. Additionally, some LBFs may pass through inland stations undetected by the algorithm as noted by Hughes and Veron (2018), especially when they move slowly and warm over land, thereby failing to meet the algorithm's temperature criteria. Besides proximity, LBF frequency also varies by coastal sector, reflecting localized influences on breeze development and propagation.
4) Most LBFs occur from early afternoon at coastal stations to late evening at the furthest stations. The relatively late onset at coastal stations suggests a weak thermal contrast between the lake and surrounding land. Peak arrival times range between 1200 and 1300 LT for coastal stations, shifting with increasing distance inland, and averaging between 1400 and 1500 LT across most stations. Dissipation typically occurs around 1730 LT at the furthest stations. These timing patterns align with the findings of Datta (1981) over the region, confirming that proximity to the coastline strongly influences LBF timing.
5) LBFs propagate fastest westward of LV at 8 m s^{-1} and slowest northward at an average speed of 5.7 m s^{-1},

indicating a directional variation in inland movement. This variation, which decreases progressively in a clockwise direction from west to east, highlights the influence of the prevailing easterly background flow on frontal speed. Similar patterns have been observed elsewhere (e.g., Baker et al. 2001), where LBs propagate inland faster when synoptic winds align with the low-level breeze flow.

Despite these directional differences in speed, LBFs can penetrate up to ~132 km inland in all directions, consistent with findings of Woodhams et al. (2019).

6) The LB exhibits weak frontal properties, with mean temperature drops of 0.75°–0.80°C, dewpoint increases of 0.7°–0.85°C, relative humidity increases of 5%–8%, and wind speed increases of 0.65–0.85 m s^{-1}, depending on the direction of propagation.

The development of the OLBDA presented in this article represents a significant advancement in the analysis of LBFs and other local meteorological phenomena over the LVB, with potential applications in disaster response and recovery. Unlike region-specific developed algorithms (e.g., Hughes and Veron 2018; Ferdiansyah et al. 2020; Viner et al. 2021), OLBDA uses percentile-based thresholds in its detection criteria, making it adaptable across regions. Additionally, the algorithm can be applied to various gridded datasets with minor tuning. However, like other algorithms, its sensitivity to wind direction signals may lead to its underperformance in capturing the total LBF occurrences at some stations. In addition, the use of 2-m wind measurements from the AWSs instead of the standard 10-m height introduces uncertainty in the wind-based criterion and may significantly affect the number of LBF passages detected. A further limitation arises from exclusion of cold pool passages by relying solely on precipitation at a station, which is not optimal since rainfall may have occurred away from the station.

When verifying the skill of OLBDA, it is important to clarify what we defined as "truth" in this study. We defined truth as LB and non-LB days identified visually from satellite imagery as described in section 3a. Because the satellite-based reference dataset relied on only a limited number of daily overpasses, this temporal sampling limitation may have affected the representativeness of both the LB and non-LB classifications. Since only a few overpasses were available, with at most three overpasses a day, LB events that occurred outside these times may have been missed, leading to some true LB days to be categorized as non-LB days, and thereby inflating the number of false alarms. This means that we would expect even a much better performance of the OLBDA. Additionally, because days with either clear skies or extensive cloud cover were classified as non-LB days in this study, the number of false alarms is most likely further overestimated. Nevertheless, it was the only feasible option available for constructing a reference dataset. We therefore consider the verification of OLBDA using visually identified LB days to be reasonable, though not perfect, and this limitation should be kept in mind when interpreting the algorithm's performance.

Our analysis provides refined insights into LBF behavior over LV and reinforces earlier findings. The observed peak arrival times of 1200–1300 LT at coastal stations and 1500–1600 LT inland reflect the weak lake–land temperature gradient, a well-known peculiarity of the LLB system in this region. These timings are broadly consistent with previous studies reporting predominantly afternoon lake breezes (Flohn and Fraedrich 1966; Datta 1981; Woodhams et al. 2019; Van de Walle et al. 2020; Odongo et al. 2022). The observed LBF penetration of up to ~132 km inland at speeds of 5.7–8.0 m s^{-1} also agrees with simulation results of Woodhams et al. (2019). Overall, the weak thermal contrast explains the generally weak frontal properties and modest temperature drops (~0.75°C), underscoring the complexity of identifying LBs in this region and the tropics compared to midlatitudes, where drops often exceed 3°C.

Although this study does not focus exclusively on precipitation-producing events, LBFs are fundamental components of the mesoscale circulation system over Lake Victoria, shaping boundary layer structure, local wind regimes, humidity gradients, and the thermodynamic environment that can favor convective initiation, even on nonprecipitating days. Their objective identification therefore contributes to a more comprehensive understanding of regional mesoscale dynamics and offers a physically grounded benchmark for evaluating numerical weather prediction and climate models. In addition, because LBFs modulate conditions relevant to air quality, heat stress, and the preconditioning of the atmosphere for subsequent convection, their detection provides broader utility beyond rainfall-focused applications.

Given the sparse network of weather stations capable of monitoring LBs in some areas across the LVB, it would be interesting to see how this OLBDA performs when applied to various model outputs, such as ECMWF Integrated Forecasting System (IFS) operational analysis dataset at 9-km spatial resolution. Studies like Hawbecker and Knievel (2022) have shown that observation-based detection algorithms underperform when applied to model outputs. Alternatively, radar data that offer higher spatiotemporal resolution and better proxy of precipitation and winds could also be explored if available. The Uganda Meteorological Services has recently installed three operational radars, including one at Entebbe International Airport along the shores of Lake Victoria; however, data were not available for this study and, even if available, would not be long enough to give robust findings. Furthermore, large-eddy simulations with a state-of-the-art NWP model have the potential to improve the understanding of the dynamical nature of LBs over the northern shores of LV and generally the impacts of LBFs on local climate and its predictability.

Acknowledgments. M. S. was supported by the DAAD Ph.D. fellowship program. The authors thank TAHMO and UDMS for providing the AWS data used in this study.

Data availability statement. The automatic weather station data were obtained from two sources (i.e., TAHMO and UDMS) and are not publicly available. For more information about TAHMO data, please visit https://tahmo.org/climate-data/. Interested parties may contact info@tahmo.com for this data. Data from UDMS stations can be obtained from UDMS upon request. Satellite imagery data were accessed from EOSDIS Worldview at https://worldview.earthdata.nasa.gov/, provided by NASA without a license on an unrestricted basis.

REFERENCES

Abatan, A. A., B. J. Abiodun, and B. J. Omotosho, 2014: On the characteristics of sea breezes over Nigerian coastal region. *Theor. Appl. Climatol.*, **116**, 93–102, https://doi.org/10.1007/s00704-013-0931-z.

Anyah, R. O., F. H. M. Semazzi, and L. Xie, 2006: Simulated physical mechanisms associated with climate variability over Lake Victoria basin in East Africa. *Mon. Wea. Rev.*, **134**, 3588–3609, https://doi.org/10.1175/MWR3266.1.

Azorin-Molina, C., D. Chen, S. Tijm, and M. Baldi, 2011: A multi-year study of sea breezes in a Mediterranean coastal site: Alicante (Spain). *Int. J. Climatol.*, **31**, 468–486, https://doi.org/10.1002/joc.2064.

Baker, R. D., B. H. Lynn, A. Boone, W.-K. Tao, and J. Simpson, 2001: The influence of soil moisture, coastline curvature, and land-breeze circulations on sea-breeze-initiated precipitation. *J. Hydrometeor.*, **2**, 193–211, https://doi.org/10.1175/1525-7541(2001)002<0193:TIOSMC>2.0.CO;2.

Barry, R. G., and R. J. Chorley, 2010: *Atmosphere, Weather, and Climate*. 9th ed. Routledge Publishing, 516 pp.

Berri, G. J., and M. Dezzutti, 2020: A sea-breeze case study in the La Plata River region using local observations, satellite images, and model simulations. *Bound.-Layer Meteor.*, **177**, 123–147, https://doi.org/10.1007/s10546-020-00548-3.

Birch, C. E., M. J. Roberts, L. Garcia-Carreras, D. Ackerley, M. J. Reeder, A. P. Lock, and R. Schiemann, 2015: Sea-breeze dynamics and convection initiation: The influence of convective parameterization in weather and climate model biases. *J. Climate*, **28**, 8093–8108, https://doi.org/10.1175/JCLI-D-14-00850.1.

Borne, K., D. Chen, and M. Nunez, 1998: A method for finding sea breeze days under stable synoptic conditions and its application to the Swedish west coast. *Int. J. Climatol.*, **18**, 901–914, https://doi.org/10.1002/(SICI)1097-0088(19980630)18:8<901::AID-JOC295>3.3.CO;2-6.

Chamberlain, J. M., C. L. Bain, D. F. A. Boyd, K. McCourt, T. Butcher, and S. Palmer, 2014: Forecasting storms over Lake Victoria using a high resolution model. *Meteor. Appl.*, **21**, 419–430, https://doi.org/10.1002/met.1403.

Cosby, A. G., V. Lebakula, C. N. Smith, D. W. Wanik, K. Bergene, A. N. Rose, D. Swanson, and D. E. Bloom, 2024: Accelerating growth of human coastal populations at the global and continent levels: 2000–2018. *Sci. Rep.*, **14**, 22489, https://doi.org/10.1038/s41598-024-73287-x.

Dai, A., F. Giorgi, and K. E. Trenberth, 1999: Observed and model-simulated diurnal cycles of precipitation over the contiguous United States. *J. Geophys. Res.*, **104**, 6377–6402, https://doi.org/10.1029/98JD02720.

Damato, F., O. Planchon, and V. Dubreuil, 2003: A remote-sensing study of the inland penetration of sea-breeze fronts from the English Channel. *Weather*, **58**, 219–226, https://doi.org/10.1256/wea.50.02.

Datta, R. K., 1981: Certain aspects of monsoonal precipitation dynamics over Lake Victoria. *Monsoon Dynamics*, J. Lighthill and R. P. Pearce, Eds., Cambridge University Press, 333–350.

Deroubaix, A., and Coauthors, 2019: Diurnal cycle of coastal anthropogenic pollutant transport over southern West Africa during the DACCIWA campaign. *Atmos. Chem. Phys.*, **19**, 473–497, https://doi.org/10.5194/acp-19-473-2019.

Diem, J. E., B. L. Konecky, J. Salerno, and J. Hartter, 2019: Is equatorial Africa getting wetter or drier? Insights from an evaluation of long-term, satellite-based rainfall estimates for western Uganda. *Int. J. Climatol.*, **39**, 3334–3347, https://doi.org/10.1002/joc.6023.

El-Geziry, T. M., M. Elbessa, and K. M. Tonbol, 2021: Climatology of sea–land breezes along the southern coast of the Levantine Basin. *Pure Appl. Geophys.*, **178**, 1927–1941, https://doi.org/10.1007/s00024-021-02726-x.

Ferdiansyah, M. R., A. Inagaki, and M. Kanda, 2020: Detection of sea-breeze inland penetration in the coastal-urban region using geostationary satellite images. *Urban Climate*, **31**, 100586, https://doi.org/10.1016/j.uclim.2020.100586.

Finney, D. L., J. H. Marsham, D. P. Rowell, E. J. Kendon, S. O. Tucker, R. A. Stratton, and L. S. Jackson, 2020: Effects of explicit convection on future projections of mesoscale circulations, rainfall, and rainfall extremes over eastern Africa. *J. Climate*, **33**, 2701–2718, https://doi.org/10.1175/JCLI-D-19-0328.1.

Flohn, H., and K. Fraedrich, 1966: Tagesperiodische zirkulation und niederschlagsverteilung am Victoria-see (Ostafrika) (The daily periodic circulation and distribution of rainfall over Lake Victoria). *Meteor. Rundsch.*, **19**, 157–165.

Fu, S., R. Rotunno, and H. Xue, 2022: Convective updrafts near sea-breeze fronts. *Atmos. Chem. Phys.*, **22**, 7727–7738, https://doi.org/10.5194/acp-22-7727-2022.

Guedje, F. K., A. V. V. Houeto, E. B. Houngninou, A. H. Fink, and P. Knippertz, 2019: Climatology of coastal wind regimes in Benin. *Meteor. Z.*, **28**, 23–39, https://doi.org/10.1127/metz/2019/0930.

Hannak, L., P. Knippertz, A. H. Fink, A. Kniffka, and G. Pante, 2017: Why do global climate models struggle to represent low-level clouds in the West African summer monsoon? *J. Climate*, **30**, 1665–1687, https://doi.org/10.1175/JCLI-D-16-0451.1.

Hastings, D. A., and Coauthors, 1999: The Global Land One-kilometer Base Elevation (GLOBE) digital elevation model, version 1.0. NOAA National Geophysical Data Centre, accessed 4 June 2025, https://www.ngdc.noaa.gov/mgg/topo/globe.html.

Hawbecker, P., and J. C. Knievel, 2022: An algorithm for detecting the Chesapeake Bay breeze from mesoscale NWP model output. *J. Appl. Meteor. Climatol.*, **61**, 61–75, https://doi.org/10.1175/JAMC-D-21-0097.1.

Hoeller, J., J. O. Haerter, and N. A. Da Silva, 2024: Characteristics of station-derived convective cold pools over equatorial Africa. *Geophys. Res. Lett.*, **51**, e2023GL107308, https://doi.org/10.1029/2023GL107308.

Hughes, C. P., and D. E. Veron, 2018: A characterization of the Delaware sea breeze using observations and modeling. *J. Appl. Meteor. Climatol.*, **57**, 1405–1421, https://doi.org/10.1175/JAMC-D-17-0186.1.

IPCC, 2023: *Climate Change 2022: Mitigation of Climate Change.* Cambridge University Press, 2030 pp., https://doi.org/10.1017/9781009157926.

Laird, N. F., D. A. R. Kristovich, X.-Z. Liang, R. W. Arritt, and K. Labas, 2001: Lake Michigan lake breezes: Climatology, local forcing, and synoptic environment. *J. Appl. Meteor.*, **40**, 409–424, https://doi.org/10.1175/1520-0450(2001)040<0409:LMLBCL>2.0.CO;2.

Loughner, C. P., D. J. Allen, K. E. Pickering, D.-L. Zhang, Y.-X. Shou, and R. R. Dickerson, 2011: Impact of fair-weather cumulus clouds and the Chesapeake Bay breeze on pollutant

transport and transformation. *Atmos. Environ.*, **45**, 4060–4072, https://doi.org/10.1016/j.atmosenv.2011.04.003.
——, and Coauthors, 2014: Impact of bay-breeze circulations on surface air quality and boundary layer export. *J. Appl. Meteor. Climatol.*, **53**, 1697–1713, https://doi.org/10.1175/jamc-d-13-0323.1.
Lumb, F. E., 1970: Topographic influences on thunderstorm activity near Lake Victoria. *Weather*, **25**, 404–410, https://doi.org/10.1002/j.1477-8696.1970.tb04129.x.
Macharia, D., K. Fankhauser, J. S. Selker, J. C. Neff, and E. A. Thomas, 2022: Validation and intercomparison of satellite-based rainfall products over Africa with TAHMO in situ rainfall observations. *J. Hydrometeor.*, **23**, 1131–1154, https://doi.org/10.1175/JHM-D-21-0161.1.
Mapes, B. E., T. T. Warner, M. Xu, and A. J. Negri, 2003a: Diurnal patterns of rainfall in northwestern South America. Part I: Observations and context. *Mon. Wea. Rev.*, **131**, 799–812, https://doi.org/10.1175/1520-0493(2003)131<0799:dporin>2.0.co;2.
——, ——, and ——, 2003b: Diurnal patterns of rainfall in northwestern South America. Part III: Diurnal gravity waves and nocturnal convection offshore. *Mon. Wea. Rev.*, **131**, 830–844, https://doi.org/10.1175/1520-0493(2003)131<0830:DPORIN>2.0.CO;2.
Mazzuca, G. M., K. E. Pickering, D. A. New, J. Dreessen, and R. R. Dickerson, 2019: Impact of bay breeze and thunderstorm circulations on surface ozone at a site along the Chesapeake Bay 2011–2016. *Atmos. Environ.*, **198**, 351–365, https://doi.org/10.1016/j.atmosenv.2018.10.068.
McCabe, E. J., and J. M. Freedman, 2023: Development of an objective methodology for identifying the sea-breeze circulation and associated low-level jet in the New York Bight. *Wea. Forecasting*, **38**, 571–589, https://doi.org/10.1175/WAF-D-22-0119.1.
Miller, S. T. K., B. D. Keim, R. W. Talbot, and H. Mao, 2003: Sea breeze: Structure, forecasting, and impacts. *Rev. Geophys.*, **41**, 1011, https://doi.org/10.1029/2003RG000124.
Muppa, S. K., V. K. Anandan, K. A. Kesarkar, S. V. B. Rao, and P. N. Reddy, 2012: Study on deep inland penetration of sea breeze over complex terrain in the tropics. *Atmos. Res.*, **104–105**, 209–216, https://doi.org/10.1016/j.atmosres.2011.10.007.
Ngoma, H., W. Wen, M. Ojara, and B. Ayugi, 2021: Assessing current and future spatiotemporal precipitation variability and trends over Uganda, East Africa, based on CHIRPS and regional climate model datasets. *Meteor. Atmos. Phys.*, **133**, 823–843, https://doi.org/10.1007/s00703-021-00784-3.
Nicholson, S. E., 1996: A review of climate dynamics and climate variability in eastern Africa. *The Limnology, Climatology and Paleoclimatology of the East African Lakes*, T.C. Johnson and E.O. Odada, Eds., Gordon and Breach Publishers, 25–56.
——, 2017: Climate and climatic variability of rainfall over eastern Africa. *Rev. Geophys.*, **55**, 590–635, https://doi.org/10.1002/2016RG000544.
Noble, S., B. Viner, and J. Wermter, 2024: Summary of atmospheric characteristics of days with inland penetrating sea breezes from 2015 to 2021. *Atmos. Sci. Lett.*, **25**, e1192, https://doi.org/10.1002/asl.1192.
Odongo, R. I., B. A. Ogwang, J. Kisembe, and H. N. Ngoma, 2022: An observational study of lake breeze over the Victoria basin in Uganda. *North Amer. Acad. Res.*, **5**, 109–123.
Papanastasiou, D. K., and D. Melas, 2009: Climatology and impact on air quality of sea breeze in an urban coastal environment. *Int. J. Climatol.*, **29**, 305–315, https://doi.org/10.1002/joc.1707.
Pietroiusti, R., and Coauthors, 2024: Possible role of anthropogenic climate change in the record-breaking 2020 Lake Victoria levels and floods. *Earth Syst. Dyn.*, **15**, 225–264, https://doi.org/10.5194/esd-15-225-2024.
Planchon, O., F. Damato, V. Dubreuil, and P. Gouery, 2006: A method of identifying and locating sea-breeze fronts in north-eastern Brazil by remote sensing. *Meteor. Appl.*, **13**, 225–234, https://doi.org/10.1017/S1350482706002283.
Ryznar, E., and J. S. Touma, 1981: Characteristics of true lake breezes along the eastern shore of Lake Michigan. *Atmos. Environ.*, **15**, 1201–1205, https://doi.org/10.1016/0004-6981(81)90311-5.
Schrage, J. M., and A. H. Fink, 2012: Nocturnal continental low-level stratus over tropical West Africa: Observations and possible mechanisms controlling its onset. *Mon. Wea. Rev.*, **140**, 1794–1809, https://doi.org/10.1175/MWR-D-11-00172.1.
Semazzi, F., 2011: Enhancing safety of navigation and efficient exploitation of natural resources over Lake Victoria and its basin by strengthening meteorological services on the lake. North Carolina State University Climate Modeling Laboratory Tech. Rep., 104 pp.
Sikora, T. D., G. S. Young, and M. J. Bettwy, 2010: Analysis of the western shore Chesapeake Bay bay-breeze. *Natl. Wea. Dig.*, **34**, 55–65.
Sills, D. M. L., J. R. Brook, I. Levy, P. A. Makar, J. Zhang, and P. A. Taylor, 2011: Lake breezes in the southern Great Lakes region and their influence during BAQS-Met 2007. *Atmos. Chem. Phys.*, **11**, 7955–7973, https://doi.org/10.5194/acp-11-7955-2011.
Simpson, J. E., 1994: *Sea Breeze and Local Winds*. Cambridge University Press, 234 pp.
Small, C., and J. E. Cohen, 2004: Continental physiography, climate, and the global distribution of human population. *Curr. Anthropol.*, **45**, 269–277, https://doi.org/10.1086/382255.
Song, Y., F. H. M. Semazzi, L. Xie, and L. J. Ogallo, 2004: A coupled regional climate model for the Lake Victoria basin of East Africa. *Int. J. Climatol.*, **24**, 57–75, https://doi.org/10.1002/joc.983.
Stauffer, R. M., and A. M. Thompson, 2015: Bay breeze climatology at two sites along the Chesapeake Bay from 1986–2010: Implications for surface ozone. *J. Atmos. Chem.*, **72**, 355–372, https://doi.org/10.1007/s10874-013-9260-y.
——, and Coauthors, 2015: Bay breeze influence on surface ozone at Edgewood, MD during July 2011. *J. Atmos. Chem.*, **72**, 335–353, https://doi.org/10.1007/s10874-012-9241-6.
Thiery, W., E. L. Davin, H.-J. Panitz, M. Demuzere, S. Lhermitte, and N. van Lipzig, 2015: The impact of the African Great Lakes on the regional climate. *J. Climate*, **28**, 4061–4085, https://doi.org/10.1175/JCLI-D-14-00565.1.
——, ——, S. I. Seneviratne, K. Bedka, S. Lhermitte, and N. P. M. van Lipzig, 2016: Hazardous thunderstorm intensification over Lake Victoria. *Nat. Commun.*, **7**, 12786, https://doi.org/10.1038/ncomms12786.
Thompson, W. T., T. Holt, and J. Pullen, 2007: Investigation of a sea breeze front in an urban environment. *Quart. J. Roy. Meteor. Soc.*, **133**, 579–594, https://doi.org/10.1002/qj.52.
van de Giesen, N., R. Hut, and J. Selker, 2014: The Trans-African Hydro-Meteorological Observatory (TAHMO). *Wiley Interdiscip. Rev.: Water*, **1**, 341–348, https://doi.org/10.1002/wat2.1034.
Van de Walle, J., W. Thiery, O. Brousse, N. Souverijns, M. Demuzere, and N. P. M. van Lipzig, 2020: A convection-permitting model for the Lake Victoria Basin: Evaluation and insight into the mesoscale versus synoptic atmospheric

dynamics. *Climate Dyn.*, **54**, 1779–1799, https://doi.org/10.1007/s00382-019-05088-2.

van der Linden, R., A. H. Fink, and R. Redl, 2015: Satellite-based climatology of low-level continental clouds in southern West Africa during the summer monsoon season. *J. Geophys. Res. Atmos.*, **120**, 1186–1201, https://doi.org/10.1002/2014JD022614.

Viner, B., S. Noble, J.-H. Qian, D. Werth, P. Gayes, L. Pietrafesa, and S. Bao, 2021: Frequency and characteristics of inland advecting sea breezes in the southeast United States. *Atmosphere*, **12**, 950, https://doi.org/10.3390/atmos12080950.

Virts, K. S., and S. J. Goodman, 2020: Prolific lightning and thunderstorm initiation over the Lake Victoria basin in East Africa. *Mon. Wea. Rev.*, **148**, 1971–1985, https://doi.org/10.1175/MWR-D-19-0260.1.

Wainwright, C. M., D. L. Finney, M. Kilavi, E. Black, and J. H. Marsham, 2021: Extreme rainfall in East Africa, October 2019–January 2020 and context under future climate change. *Weather*, **76**, 26–31, https://doi.org/10.1002/wea.3824.

Waniha, P. F., R. D. Roberts, J. W. Wilson, A. Kijazi, and B. Katole, 2019: Dual-polarization radar observations of deep convection over Lake Victoria Basin in East Africa. *Atmosphere*, **10**, 706, https://doi.org/10.3390/atmos10110706.

Warner, T. T., B. E. Mapes, and M. Xu, 2003: Diurnal patterns of rainfall in northwestern South America. Part II: Model simulations. *Mon. Wea. Rev.*, **131**, 813–829, https://doi.org/10.1175/1520-0493(2003)131<0813:DPORIN>2.0.CO;2.

Watts, A. J., 1955: Sea breeze at Thorney Island. *Meteor. Mag.*, **84**, 42–48.

Wentworth, G. R., J. G. Murphy, and D. M. L. Sills, 2015: Impact of lake breezes on ozone and nitrogen oxides in the greater Toronto area. *Atmos. Environ.*, **109**, 52–60, https://doi.org/10.1016/j.atmosenv.2015.03.002.

Wermter, J., S. Noble, and B. Viner, 2022: Impacts of the thermal gradient on inland advecting sea breezes in the southeastern United States. *Atmosphere*, **13**, 1004, https://doi.org/10.3390/atmos13071004.

Wilson, J., and R. D. Roberts, 2022: Lake Victoria thunderstorms: Radar-observed initiation and storm evolution modes. *Mon. Wea. Rev.*, **150**, 2485–2502, https://doi.org/10.1175/MWR-D-21-0283.1.

WMO, 2025: State of the climate in Africa 2024. World Meteorological Organization Rep. WMO- 1370, 22 pp., https://doi.org/10.18356/9789263113702.

Woodhams, B. J., C. E. Birch, J. H. Marsham, T. P. Lane, C. L. Bain, and S. Webster, 2019: Identifying key controls on storm formation over the Lake Victoria basin. *Mon. Wea. Rev.*, **147**, 3365–3390, https://doi.org/10.1175/MWR-D-19-0069.1.

——, and Coauthors, 2022: Aircraft observations and sub-km modelling of the lake–land breeze circulation over Lake Victoria. *Quart. J. Roy. Meteor. Soc.*, **148**, 557–580, https://doi.org/10.1002/qj.4155.

Zhang, F., N. Bei, J. W. Nielsen-Gammon, G. Li, R. Zhang, A. Stuart, and A. Aksoy, 2007: Impacts of meteorological uncertainties on ozone pollution predictability estimated through meteorological and photochemical ensemble forecasts. *J. Geophys. Res.*, **112**, D04304, https://doi.org/10.1029/2006JD007429.